POLITECNICO DI TORINO

Master degree course in Mechatronic Engineering

Master Degree Thesis

Vehicle dynamics performance assessment by development of model-supported testing

Academic Supervisor
Prof. Stefano Alberto Malan

Candidate
Ludovico Ruga
s255243

Company Supervisor
Siemens Industry Software NV
Dr. Tom Dirickx

Academic year 2018-2019

Abstract

The research field of virtual sensing looks for techniques to provide access to difficult-to-measure quantities. This is done by combining existing measurement data with model information. The presented work focuses on the estimation of the vehicle sideslip angle and of the forces exchanged at road level. Accurate estimation of vehicle motion during handling maneuvers can be achieved by the development of model-supported testing. The presented approach uses both a fixed parameter linear tire model, and an adaptive linear tire model together in an Extended Kalman Filter. The former model is used to provide an additional virtual measurement, and a reliable reference during straight driving, whereas the latter accounts for variable tire behavior. A phase error in the estimated sideslip angle, due to vehicle motion being considered only on the horizontal plane, is corrected by considering the contribution of the roll rate. The proposed approach provides deeper insight in vehicle performance with a reduced test setup, through the enhancement of low qualities responses and the estimation of additional quantities.

Contents

List of Figures

List of Tables

Chapter 1

Introduction

1.1 General problem

The subject of "vehicle dynamics" is the study of the vehicle responses to driver inputs on a road surface. It has always been of paramount importance for automotive companies since it has a central role in the design of the vehicle, with the purpose of improving safety and comfort, as well as performance. This can be achieved by analyzing quantities such as forces, velocities and accelerations at precise locations of the automobile; such quantities are usually obtained with physical sensors. Although current measurement methods are reliable and yield precise results in most conditions, they have two major problems: the measurement equipment used, such as force transducers, IMUs (Inertial Measurement Unit), optical sensors and strain gauges, is very expensive, and the process of acquiring these data and analyzing them is requires a long time. Moreover, in many practical applications, placing the sensors at the desired location can be very challenging, if not impossible. In order to overcome these issues, virtual sensors are developed to estimate the values that were previously measured by physical sensors. Virtual sensing techniques are based on the concept that, by combining a reduced amount of measured data with model information, one can get access to a wider set of values or improve the quality of the data with reduced measurement effort. Virtual sensing can be applied to different areas, such as computer science, wireless networking, remote sensing, chemistry, aerospace or automotive. For example, aircraft, satellites or ship crafts equipped with physical sensing devices that acquire information from a given area. Virtual sensing techniques are broadly applicable and enable one to predict or estimate information at one location from the data measured at other locations. In short, virtual sensing is to use physical sensing data and a suitable model to obtain the desired values in the areas of interest without putting real sensors or directly contacting the object [1]. In the automotive field, these methodologies can be used to determine the tire contact forces with the road or other difficult to measure but important quantities such as the vehicle sideslip angle.

1.2 State of the art

Virtual sensors, also known as soft sensors, estimator or observers, have been a topic of interest in the past decades and have been used in practical applications in different areas. In this section a review of some of the applications of virtual sensors is given.
In [2], Cathey and Dailey developed a traffic management system with the ability to create real-time traffic speed information by using virtual sensors that are based on transit vehicle data. This project harvests existing automatic vehicle location and transports the data to the University of Washington, where a series of operations converts it into roadway speed information, which is used to reflect traffic congestion. The resulting traffic data product is then provided to the Washington State Department of Transportation as a virtual sensor data source for roadways where there are no physical sensors from which one can obtain information.
In process industries, virtual sensors are used to measure the concentration of certain components or in gas sensing systems with high sensitivity. A low power virtual sensor array based on a micro-machined gas sensor for fast discrimination between H_2, CO and relative humidity, to be used for air quality control, explosion warning or leak detection in chemical warehouses, is presented in [3]. In [4], Schütze and Gramm propose a virtual multisensor system for the identification of organic solvent to be used in leak detection systems.
In the field of mobile robots, virtual sensing techniques are used by Bellas et al. [5] at the sensing level to increase the accuracy of sensing information. An Artificial neural network is established, and it is used with time delays as virtual sensors. The virtual sensor outputs are estimated through a temporal correlation of real sensing values. This method can increase the response accuracy of mobile robots.
In the automotive field, estimators and observers have been widely used to estimate variables which are not directly measurable. In [6], the velocity of the center of mass of the vehicle is obtained via a fusion of the data from all rotational wheel velocities and the longitudinal acceleration physical sensor using a Kalman filter approach. An estimator for the yaw rate is also presented, to solve the issue of offset drift in gyroscopes caused by temperature changes. In order to increase the accuracy of the measured yaw rate, signals from different sensors are combined to obtain the yaw rate. Their weights are determined according to the driving situation. In this procedure, a fuzzy estimator based on heuristic knowledge is used. More recently, Avino et al. [7] proposed an accident prevention system which, through the use of virtual sensing, merges the output of on-board vehicles sensors and smart city sensors to distribute real-time information to increase the awareness of the surrounding environment.

1.3 Problem statement

This thesis work, which has been developed in collaboration with Siemens PLM Software, aims to develop a modular vehicle estimator based on simplified models and selected measurements. The estimator is based on an Extended Kalman Filter, in which data measured at the center of gravity of the vehicle is combined with a single track model to improve the quality of the signals as well as to obtain quantities which are not directly measured. The most relevant outputs of the estimator are:

- Lateral velocity
- Vehicle body sideslip angle
- Axle lateral loads
- Wheel vertical loads
- Wheel lateral loads
- Tire slip angles

The objective of this project is to find an alternative to the current test-based approaches which, although detailed, are too elaborate and expensive. Moreover, it also aims to improve the quality of the signals obtained in challenging conditions, such as low lateral acceleration maneuvers, in which the lateral acceleration is below $0.1g$. In this condition, most of the physical sensors used in automotive companies, such as accelerometers and gyroscopes, should work in their noise band [8]. Another issue that arises with low levels of lateral acceleration is that many un-modeled non-linear phenomena, whose effect can be neglected at medium and high level of lateral acceleration, make the estimation of vehicle parameters very complicated. The study of a vehicle's response for these type of maneuvers is very important due to their effect on the driver's perception of the vehicle motion and on the precision and quickness of the reaction to inputs. The driving situations in which the vehicle is subject to levels of lateral acceleration lower than $0.1g$ are also known as on-center steering conditions. A typical situation is driving at high speed on an highway on a straight road: the lateral acceleration in this scenario is close to zero, and if the vehicle ha poor on-center handling behavior, steering inputs are continuously needed [9].
The starting point for this thesis project is the estimator presented in [10], developed for control applications, which has been adapted for vehicle dynamics analysis purposes and amplified. The work done at Siemens by previous students in [11] and [8] has also been very useful and is referenced throughout the following chapters. Particular emphasis has been put on the modular properties of the estimator: if the number of inputs is increased by introducing additional parameters or measurements, new signals are obtained and the quality of the signals already present is

improved. The proposed approach has been tested with data from two commercial vehicle and from the SimRod (figure 1.1), an electric vehicle developed by Siemens for testing purposes.

Figure 1.1: SimRod vehicle

1.4 Thesis outline

Chapter 2 initiates the discussion of lateral dynamics by introducing the tire and vehicle models, in order to provide the knowledge about the states and parameters which are addressed in later chapters. The addressed vehicle models are the single-track and the two-track models, while the linear tire model and the adaptive linear tire model are presented as wheel models.

Chapter 3 provides the needed theoretical background about the estimation techniques applied in the proposed approach. The two approaches discussed are Kalman filters, used in the vehicle dynamics estimation, and the Linear Matrix Inequalities approach, used to implement the steering angle estimator.

Chapter 4 introduces the complete structure of the estimator, illustrating which inputs are needed and which outputs can be obtained. Then, a detailed explanation of the development steps and characteristics is provided for each block of the modular estimator.

Chapter 5 provides an overview of the track tests used to validate the estimator, addressing the sensor equipment and the characteristics and parameters of the vehicle used. The handling maneuvers and test conditions are also described.

The results obtained are presented and commented in Chapter 6. Different handling maneuvers and conditions are used to validate the estimators and evaluate the limits of its performance.

Chapter 7 contains the conclusions reached during the thesis work. Suggestions for future work are provided, along with possible directions to be taken to reach new objectives, starting from the results obtained in this work.

Chapter 2

Vehicle dynamics theory

Vehicle dynamics is studied through the use of mathematical models, which can include the whole vehicle or only parts of it (tire, suspensions, power train, etc.). For the purposes of this thesis project, only tire and vehicle models are discussed here. Moreover, this chapter will focus on simplified models with only a few degrees of freedom. This is a well considered trade-off, because even though simplified models lack the ability to capture complex non-linear phenomena, they only require a limited number of easily obtainable parameters and, under some reasonable assumptions, provide fairly accurate results.

2.1 Coordinate system

Many different coordinate systems are used in the automotive industry. In order to avoid confusion, any future references to the X, Y or Z axis or to the rotations about them is to be considered in the *ISO 8855 intermediate system*, shown in figure 2.1. This frame is attached to the vehicle center of gravity, and rotates with the yaw motion of the vehicle, but not with the roll and pitch motion. The three axes are oriented as follows:

- The X axis is perpendicular to the gravity vector and points to the forward direction of the vehicle, projected on the horizontal plane.
- The Y axis is perpendicular to the gravity vector and to the X axis and is in the lateral direction of the vehicle, pointing to the left, projected on the horizontal plane.
- The Z axis is parallel to the gravity vector and positive when pointing upwards.

The roll, pitch and yaw angles are the rotations about respectively the X, Y and Z axes, with their direction being positive according to the right-hand rule. The choice of a coordinate system in which the X-Y plane is not always parallel to the

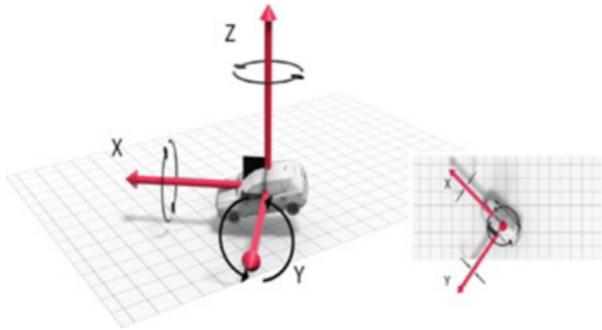

Figure 2.1: ISO 8855 intermediate system reference frame

road, as in the condition of a banking or uphill road, has been made because the modular estimator developed in this thesis is thought to be coupled with a vehicle body and road angle estimator, which could decouple the road influences from the sprung mass motion due to accelerations and lateral dynamics.

2.2 Tire model

When dealing with the dynamics of a vehicle, it is of paramount importance to have knowledge on the forces that act on the wheels. To do so, numerous tire models have been developed over the years. The most accurate ones (such as the Pacejka "magic formulas") require up to 20 coefficients [12], whereas the simpler ones, such as the linear tire model, require very few parameters. Tire models deal mostly with the lateral dynamics phenomena that appear outside of straight driving scenarios.

When a vehicle is driving in a straight line, the direction in which a wheel is traveling coincides with its heading direction. However, when the vehicle is subject to lateral and/or yaw motion, the traveling direction of the wheel can be different from its heading direction. The angle between the direction the wheel is pointing and the direction in which it is actually moving, i.e. the angle between the velocity vector of the tire v_W and the heading direction of the wheel x_W, is the tire slip angle α (figure 2.2). This is a key parameter because it has a direct relation with the wheel lateral force F_y.

As it can be seen in figure 2.3, the relationship between the lateral force and the tire slip angle is linear for small values of the slip angles. After it exceeds a certain value, the lateral force increases at a slower ratio before finally reaching a saturation value [13].

The slope of the slip-force characteristic for low values of the tire slip angle is the *cornering stiffness* C_α. In the linear tire model, the lateral force F_y is expressed by the following equation:

$$F_y(\alpha) = C_\alpha \cdot \alpha \tag{2.1}$$

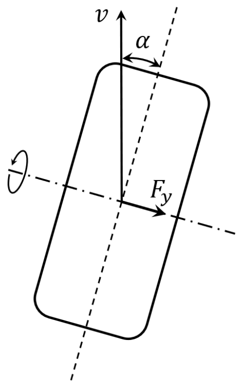

Figure 2.2: Vehicle tire in motion with slip angle

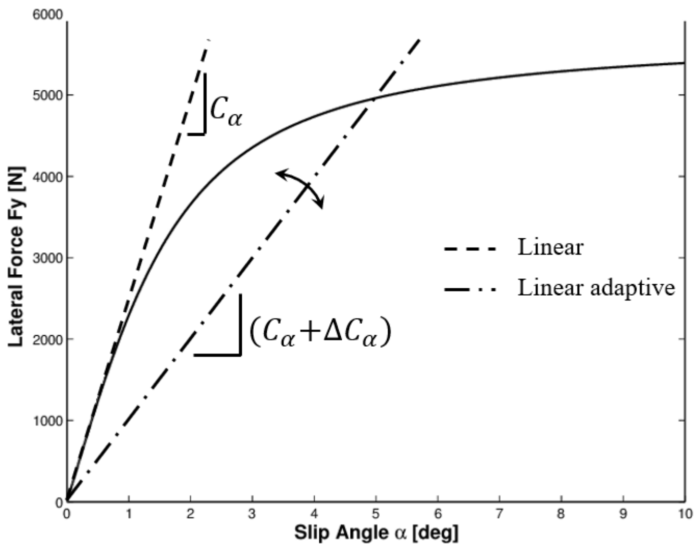

Figure 2.3: Slip-Force characteristic

where C_α is the cornering stiffness. This equation models the entire slip-force characteristic as if it were a linear relation. Due to this characteristic, the linear tire model is only accurate when dealing with small tire slip angles. Since assuming the tire slip angle to be small is reasonable in non-critical driving scenarios, this is one of the most used tire models in literature.

However, to overcome the limitations of this model, Best et al. proposed in [14] an adaptive linear model:

$$\begin{cases} F_{yi}(\alpha) = -2 \cdot C_{\alpha i} \cdot \alpha_i \\ \dot{C}_{\alpha i} = 0 \end{cases} \quad \text{for i} \in \{\text{f,r}\} \tag{2.2}$$

where $C_{\alpha i}$ is the adaptive cornering stiffness, whose variable behavior (due to non-linear tire behavior, variations in the road friction coefficient, etc.), is modeled with a random walk model.

Due to its simplicity and effectiveness even outside of the linear region of the slip-force characteristic, the adatpive linear tire model has been adopted in this thesis project.

2.3 Single track model

Several vehicle models have been developed over the years, with different degrees of complexity and number of degrees of freedom. In this project, for the development of the modular vehicle dynamics estimator the single track model is chosen (figure 2.4), also known as the bicycle model, in order to develop an observable system for a common set of automotive sensors [10].

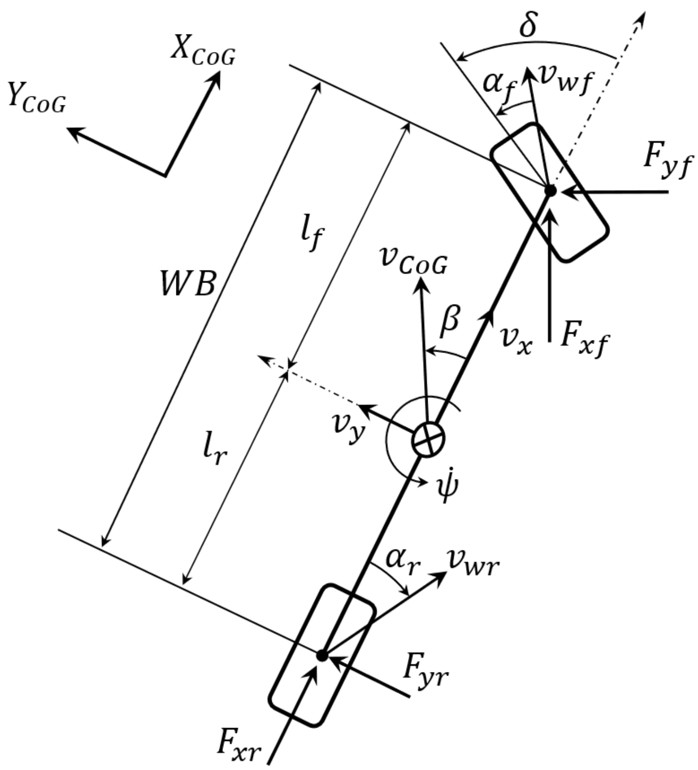

Figure 2.4: Bicycle model

In this model, the two wheels on each axle are condensed into one, with the effect of reducing the degrees of freedom to three (motion along the X and Y axes, and rotation about the Z axis), thus simplifying the state equations. The roll and pitch motion are neglected. The considered variables are:

- v_x and v_y are respectively the longitudinal and lateral velocity of the center of gravity (CoG) of the vehicle, projected into a vehicle-fixed reference frame
- v_{CoG} is the direction of the CoG velocity
- $\dot{\psi}$ is the yaw rate
- β is the vehicle CoG sideslip angle
- α_f and α_r are respectively the front and rear tire slip angles
- δ is the front wheel steering angle
- v_{wf} and v_{wr} are the front and rear wheel velocities
- F_{xf} and F_{xr} are respectively the front and rear wheel longitudinal forces, while F_{yf} and F_{yr} are the front and rear lateral forces, all expressed in a tire-fixed reference frame
- l_f and l_r are the distances from the center of gravity respectively of the front and rear axles
- WB is the wheelbase of the vehicle (i.e. the distance between the front and rear axles).

The decision to use the bicycle model has also been influenced by the consideration that, without prior assumptions on the distribution of the left and right loads, a four-wheel model would not have allowed the separation of the forces on each axle.

The states equation for the lateral vehicle dynamics in the bicycle model, can be formulated as:

$$\begin{cases} \dot{v_y} = \frac{1}{m} \cdot (F_{yf} + F_{yr}) - v_x \cdot \dot{\psi} \\ \ddot{\psi} = \frac{1}{I_{zz}} \cdot (l_f \cdot F_{yf} - l_r \cdot F_{yr}) \end{cases} \tag{2.3}$$

where m is the mass of the vehicle and I_{zz} is the yaw moment of inertia. In the above equation, the longitudinal velocity v_x appears as an input. In order to take its variation into account, v_x is transformed into a state by adding a kinematic update equation to 2.3, which then becomes:

$$\begin{cases} \dot{v_y} = \frac{1}{m} \cdot (F_{yf} + F_{yr}) - v_x \cdot \dot{\psi} \\ \ddot{\psi} = \frac{1}{I_{zz}} \cdot (l_f \cdot F_{yf} - l_r \cdot F_{yr}) \\ \dot{v_x} = a_x + v_y \cdot \dot{\psi} \end{cases} \tag{2.4}$$

where a_x is the inertial longitudinal acceleration.

The definition of the tire slip angles α_f and α_r can be obtained from figure 2.4, as they are calculated by equating the wheel and chassis velocities both in the longitudinal and lateral direction. The velocity balance equation of the front wheel in the longitudinal direction is the following:

$$\underbrace{v_{wf} \cdot \cos(\delta - \alpha_f)}_{\textit{wheel velocity}} = \underbrace{v_{CoG} \cdot \cos(\beta)}_{\textit{chassis velocity}} \tag{2.5}$$

while for the lateral direction:

$$\underbrace{v_{wf} \cdot \sin(\delta - \alpha_f)}_{\textit{wheel velocity}} = \underbrace{v_{CoG} \cdot \sin(\beta) + l_f \cdot \dot{\psi}}_{\textit{chassis velocity}} \tag{2.6}$$

By diving equation (2.6) by equation (2.5), one obtains:

$$\tan(\delta - \alpha_f) = \frac{v_{CoG} \cdot \sin(\beta) + l_f \cdot \dot{\psi}}{v_{CoG} \cdot \cos(\beta)} \tag{2.7}$$

Similarly, for the rear wheel, the balance equation for the longitudinal direction is:

$$\underbrace{v_{wr} \cdot \cos(\alpha_r)}_{\textit{wheel velocity}} = \underbrace{v_{CoG} \cdot \cos(\beta)}_{\textit{chassis velocity}} \tag{2.8}$$

and for the lateral direction,

$$\underbrace{v_{wr} \cdot \sin(\alpha_r)}_{\textit{wheel velocity}} = \underbrace{-v_{CoG} \cdot \sin(\beta) + l_r \cdot \dot{\psi}}_{\textit{chassis velocity}} \tag{2.9}$$

Dividing equation (2.9) by (2.8):

$$\tan(\alpha_r) = \frac{-v_{CoG} \cdot \sin(\beta) + l_r \cdot \dot{\psi}}{v_{CoG} \cdot \cos(\beta)} \tag{2.10}$$

In stable driving conditions, a reasonable assumption is that the tire slip angle α is usually lower than 5° [6], therefore the small angle assumption can be applied by substituting $\sin\alpha \approx \alpha$, $\cos\alpha \approx 1$ and $\tan\alpha \approx \alpha$. Equation (2.7) can then be used to express α_f:

$$\alpha_f = -\beta - \frac{l_f \cdot \dot{\psi}}{v_{CoG}} + \delta \tag{2.11}$$

While equation (2.10) becomes:

$$\alpha_r = -\beta + \frac{l_r \cdot \dot{\psi}}{v_{CoG}} \tag{2.12}$$

By substituting equations (2.11) and (2.12) in the adaptive linear tire model (2.2), and combining it with the bicycle model state equations (2.4), the following continuous time model is obtained:

$$
\begin{cases}
\dot{v_y} = \dfrac{-2(C_f + C_r)}{m \cdot v_x} v_y - \left(\dfrac{2(C_f \cdot l_f - C_r \cdot l_r)}{m \cdot v_x} + v_x \right) \dot{\psi} + \dfrac{2 \cdot C_f}{m} \delta \\
\\
\ddot{\psi} = \dfrac{-2(C_f \cdot l_f - C_r \cdot l_r)}{I_{zz} \cdot v_x} v_y - \dfrac{2(C_f \cdot l_f^2 + C_r \cdot l_r^2)}{I_{zz} \cdot v_x} \dot{\psi} + \dfrac{2 \cdot C_f \cdot l_f}{I_{zz}} \delta \\
\dot{v_x} = a_x + v_y \cdot \dot{\psi} \\
\dot{C_f} = 0 \\
\dot{C_r} = 0
\end{cases}
\tag{2.13}
$$

The final state equations (2.13) has five states, and they are used in Chapter 4 as the vehicle model for the modular estimator.

2.4 Two-track model

The model used for the tires vertical forces estimation is the two-track model (figures 2.5 and 2.6), together with a steady-state load transfer model [15]. The lateral and longitudinal load transfers are expressed as:

$$
\Delta F_{zyi} = \frac{1}{t_i} \left(\frac{c_{\phi i}}{c_{\phi f} + c_{\phi r} - m \cdot g \cdot h'} h' + \frac{WB - l_i}{WB} h_{ri} \right) m \cdot a_y \tag{2.14}
$$

for $i \in \{f, r\}$,

$$
\Delta F_{zx} = \frac{m \cdot a_x \cdot h_{CoG}}{2 \cdot WB} \tag{2.15}
$$

where:

- ΔF_{zyi} and ΔF_{zx} are respectively the lateral and longitudinal changes in the vertical loads on the left and right side of the axle,
- t_i is the axle track width,
- $c_{\phi i}$ is the axle roll stiffness,
- h_{ri} is the axle roll center height,
- h_{CoG} is the height of the center of gravity,
- h' is the difference between h_{CoG} and h_{ri}, i.e the distance between CoG and roll center,
- a_x and a_y are the vehicle CoG longitudinal and lateral accelerations.

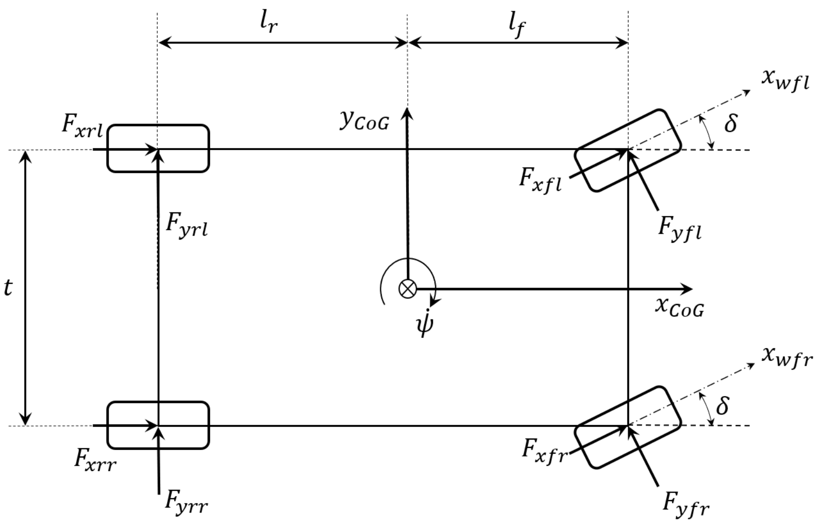

Figure 2.5: Two-track vehicle model, XY plane

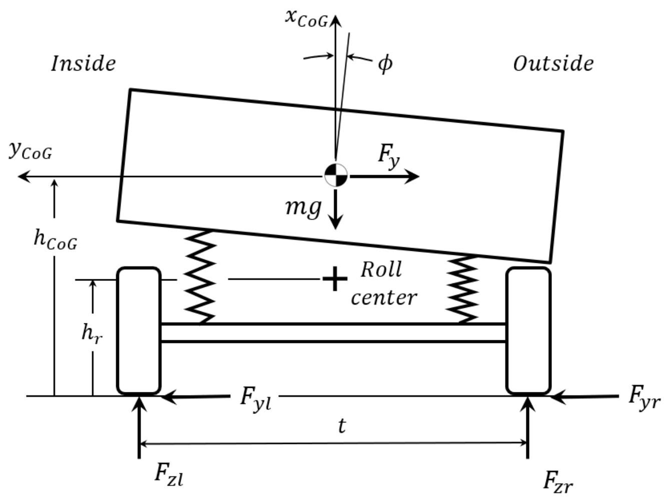

Figure 2.6: Two-track vehicle model, YZ plane

Equation (2.14) includes steady-state suspension effects, while they are neglected in (2.15) since the distribution between left and right wheel are assumed to be equal on a smooth surface [15].

The vertical loads for each wheel are then expressed by the following equations:

$$
\begin{aligned}
F_{zfl} &= \frac{m \cdot g \cdot l_r}{2 \cdot WB} - \Delta F_{zyf} - \Delta F_{zx} \\
F_{zfr} &= \frac{m \cdot g \cdot l_r}{2 \cdot WB} + \Delta F_{zyf} - \Delta F_{zx} \\
F_{zrl} &= \frac{m \cdot g \cdot l_f}{2 \cdot WB} - \Delta F_{zyr} + \Delta F_{zx} \\
F_{zrr} &= \frac{m \cdot g \cdot l_f}{2 \cdot WB} + \Delta F_{zyr} + \Delta F_{zx}
\end{aligned}
\tag{2.16}
$$

Chapter 3

Estimation theory

The estimation problem refers to the empirical evaluation of an uncertain variable, like an unknown characteristic parameter or a remote signal, by means of experimental observations and measurements of the system under investigation.

An estimation problem always assumes a mathematical model of the system. The models can be classified as:

- *static models*, characterized by instantaneous (or algebraic) relationships among variables, usually utilized in the classical statistics
- *dynamics models*, either described in *discrete-time* or *continuous-time*, characterized by relationships among variables that can be represented with differential equations

The variable to be estimated, scalar or vector, is denoted as $\theta(t)$ and can be either constant or time-varying. The available data, acquired at N uniformly distributed time instants, is denoted as $d(t)$, for $t \in T = \{t_1, t_2, ..., t_N\}$, where T is the set of observations instants, so the entire observation data set is given by:

$$d = \{d(t_1), d(t_2), ..., d(t_N)\}$$

An estimator (or estimator algorithm) is a function $f(\cdot)$ which, starting from data, returns a value for the variable to be estimated:

$$\hat{\theta}(t) = f(d)$$

where $\hat{\theta}(t)$ is called the estimate of θ, and can either be:

- *constant*. In this case the problem is denoted as a parametric identification, the estimator is denoted by $\hat{\theta}$ or by $\hat{\theta}_T$, and the true value of the unknown variable is denoted by θ_o

- a *time-varying function*. In this case the estimator is denoted by $\hat{\theta}(t|T)$ or by $\hat{\theta}(t|N)$ if the time instants for observation are uniformly distributed. Moreover, according the the relationship between t and the last time instant t_N:
  1. when $t > t_N$, it is a prediction problem;
  2. when $t = t_N$, it is a filtering problem;
  3. when $t < t_N$, it is a smoothing or interpolation problem.

3.1 Kalman filter theory

Since its first formulation by Rudolph E. Kalman in 1960 [16], the Kalman filter has long been regarded as the optimal solution for many data estimation tasks.

The Kalman filter is an algorithm that employs a set of data measured over time, which contains statistical noise and other inaccuracies, and estimates desired variables with a degree of accuracy that tends to be higher than the ones obtained using a single measurements alone, by estimating a joint probability distribution over the variables for each time step. In this section, the Kalman filtering problem will be introduced.

3.1.1 Kalman filtering problem

Let us consider a discrete-time, linear time-invariant (LTI), dynamical system $\mathcal{S}$ (figure 3.1), described by the following state space model:

$$\mathcal{S}\begin{cases} x(t+1) = Ax(t) + v_1(t) \\ y(t) = Cx(t) + v_2(t) \end{cases} \qquad t = 1,2,... \tag{3.1}$$

where $x(y) \in \mathbb{R}^n, y(t) \in \mathbb{R}^q, v_1(t) \in \mathbb{R}^n, v_2(t) \in \mathbb{R}^q$, and assume that:

- the process noise $v_1(t)$ and the measurement noise $v_2(t)$ are white noises with zero mean value and known variance which are uncorrelated to each other, i.e. $v_1(t) \sim WN(0, V_1)$ and $v_2(t) \sim WN(0, V_2)$ are such that:

$$\begin{aligned} &E[v_1(t_1)v_1(t_2)^T] = V_1\delta(t_2 - t_1) && \text{(whiteness of } v_1(t)) \\ &E[v_2(t_1)v_2(t_2)^T] = V_2\delta(t_2 - t_1) && \text{(whiteness of } v_2(t)) \\ &E[v_1(t_1)v_2(t_2)^T] = 0, \quad \forall t_1, t_2 && \text{(uncorrelation of } v_1(t) \text{ and } v_2(t)) \end{aligned}$$

- $A \in \mathbb{R}^{n\times n}, C \in \mathbb{R}^{q\times n}, V_1 \in \mathbb{R}^{n\times n}, V_2 \in \mathbb{R}^{q\times q}$ are known matrices,
- the initial state $x(t=1)$ is an unknown random vector $x(t=1) \sim (0, P_1)$, uncorrelated to noises $v_1(t)$ and $v_2(t)$,
- the output measurements $y(t)$ are available for $t = 1,2,...,N$

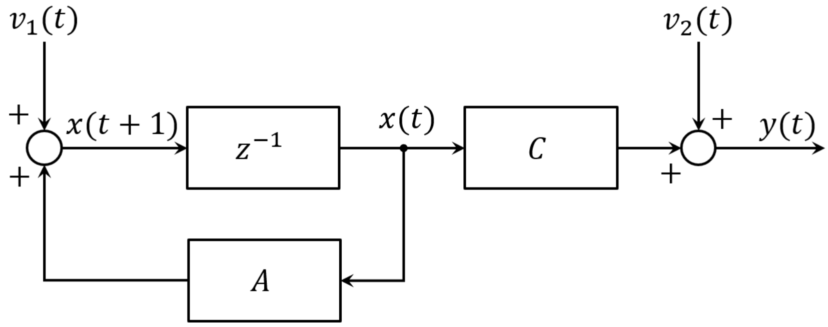

Figure 3.1: Graphical representation of the dynamical system $\mathcal{S}$

The objective is to estimate the state $x(N+r)$, where we will focus at first on $r = 1$ (one-step prediction problem) and pass on to $r = 0$ (filtering problem).

Since $v_1(t)$ and $v_2(t)$ are random variables, also $x(t)$ and $y(t)$ are too. Then, the Bayesian estimated of the state $x(N+r)$ given the N measurements $y(N), y(N-1), ..., y(1)$ is equal to:

$$\hat{x}(N+r|N) = E[x(N+r)|d] = \bar{x}(N+r) + \Sigma_{x(N+r)d}\Sigma_{dd}^{-1}(d-\bar{d}) \tag{3.2}$$

where

$$\begin{aligned}
&\bar{x}(N+r) = E[x(N+r)] \in \mathbb{R}^n, \\
&d = y^N = [y(N)^T \; y(N-1)^T \; \cdots y(1)^T]^T \in \mathbb{R}^{Nq}, \\
&\bar{d} = E[d] = E[y^N] \in \mathbb{R}^{Nq}, \\
&\Sigma_{dd} = E[(d-\bar{d})(d-\bar{d})^T] \in \mathbb{R}^{Nq\times Nq}, \\
&\Sigma_{x(N+r)d} = E[(x(N+r)-\bar{x}(N+r))(d-\bar{d})^T] \in \mathbb{R}^{n\times Nq}
\end{aligned}$$

Moreover, since $v_1(t)$ and $v_2(t)$ have zero mean value $\forall t$, also $x(y), y(t)$ must have zero mean value $\forall t$:

$$\hat{x}(N+r|N) = E[x(N+r)|y^N] = \Sigma_{x(N+r)y^N}\Sigma_{y^N y^N}^{-1} y^N \tag{3.3}$$

The main drawback of the proposed form of the Bayesian estimate (3.3) is that it requires the batch processing of the measurements, since all information is incorporated in one single step into the estimate. This leads to the necessity for inverting $\Sigma_{y^N y^N} \in \mathbb{R}^{Nq\times Nq}$, which may be a very difficult task when N is large.

To avoid this drawback, recursive or sequential estimation schemes are looked for, in which the current estimate depends on the previous estimate and the current measurement. Such schemes rely on sequential processing of data, where the measurements are processed in stages. Using the recursive Bayesian estimation method, at first the one-step prediction problem will be solved, then the filtering problem will be dealt with.

3.1.2 One-step Kalman predictor

The objective of the one-step Kalman predictor is, given the data vector $y^N = [y(N)^T\ y(N-1)^T\ ...\ y(1)^T]^T$, to find a recursive Bayesian estimate $\hat{x}(N+1|N)$ of the state $x(N+1)$ starting from the estimate $\hat{x}(N|N-1)$ of the state $x(N)$ obtained at the previous stage. The *innovation* of $y(N+1)$ given y^N is defined by:

$$e(N+1) = y(N+1) - E[y(N+1)|y^N] \in \mathbb{R}^q \tag{3.4}$$

where $E[y(N+1)|y^N]$ is the projection of $y(N+1)$ over the subspace $\mathcal{H}[y^N]$ generated by all the components of y^N, called past subspace. The innovation $e(n+1)$ is orthogonal to $\mathcal{H}[y^N]$, i.e. the innovation is orthogonal to the past (figure 3.2).

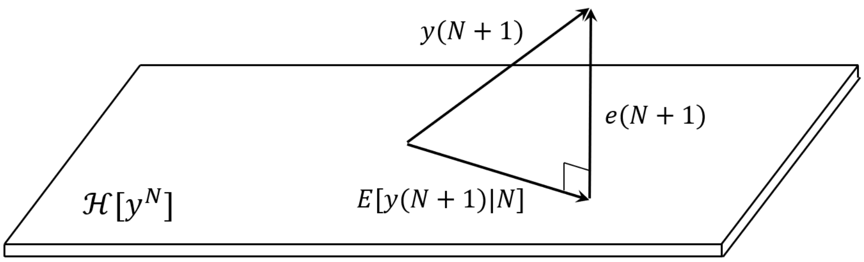

Figure 3.2: Past subspace $\mathcal{H}[y^N]$

The prediction error of the state $x(N+1)$ is defined by:

$$\tilde{x}(N+1) = x(N+1) - E[x(N+1)|y^N] \in \mathbb{R}^n \tag{3.5}$$

where $E[x(N+1)|y^N]$ is the projection of $x(N+1)$ over $\mathcal{H}[y^N]$, then $\tilde{x}(N+1)$ is orthogonal to $\mathcal{H}[y^N]$. Moreover,

$$\begin{aligned} E[\tilde{x}(N+1) &= E[x(N+1) - \Sigma_{x(N+1)y^N}\Sigma^{-1}_{y^N y^N} y^N = \\ &= E[x(N+1)] - \Sigma_{x(N+1)y^N}\Sigma^{-1}_{y^N y^N} E[y^N] = 0 \end{aligned} \tag{3.6}$$

and

$$\begin{aligned} Var[\tilde{x}(N+1)] &= E[(\tilde{x}(N+1) - E[\tilde{x}(N+1)])(\tilde{x}(N+1) - E[\tilde{x}(N+1)])^T] = \\ &= E[\tilde{x}(N+1)\tilde{x}(N+1)^T] = P(N+1) \end{aligned} \tag{3.7}$$

Since $e(N+1)$ and $\tilde{x}(N+1)$ are parallel, being both orthogonal to the past subspace $\mathcal{H}[y^N]$, they must be linearly dependent:

$$\begin{aligned}
e(N+1) &= y(N+1) - E[y(N+1)|Y^N] = \\
&= Cx(N+1) + v_2(N+1) - E[Cx(N+1) + v_2(N+1)|y^N] = \\
&= Cx(N+1) + v_2(N+1) - E[Cx(N+1)|y^N] - E[v_2(N+1)|y^N] = \\
&= Cx(N+1) - v_2(N+1) - CE[x(N+1)|y^N] - E[v_2(N+1)] = \\
&= Cx(N+1) - CE[x(N+1)|y^N] + v_2(N+1) = \\
&= C(x(N+1) - E[x(N+1|y^N]) + v_2(N+1) = \\
&= C\tilde{x}(N+1) + v_2(N+1)
\end{aligned} \tag{3.8}$$

where $E[v_2(N+1)|y^N] = E[v_2(N+1)] = 0$ since $v_2(N+1)$ is a random variable with zero mean value and independent of y^N.

The optimal estimate for the state $x(N+1)$ based on data y^N is given by:

$$\tilde{x}(N+1|N) = E[x(N+1)|y^N] = E[x(N+1)|y^{N-1}, y(N)] \tag{3.9}$$

where $y^{N-1} = [y(N-1)^T \; y(N-2)^T \cdots y(1)^T]^T \in \mathbb{R}^{(N-1)q}$. From the recursive Bayesian formula, it results that:

$$\begin{aligned}
\tilde{x}(N+1|N) &= E[x(N+1)|y^{N-1}, y(N)] = \\
&= E[x(N+1)|y^{N-1}] + E[x(n+1)|e(N)]
\end{aligned} \tag{3.10}$$

where $e(N)$ is the innovation of $y(N)$ given y^{N-1}.

From the state equation of the system $\mathcal{S}$:

$$\begin{aligned}
E[x(N+1)|y^{N-1}] &= E[Ax(N) + v_1(N)|y^{N-1}] = \\
&= AE[x(N)|y^{N-1}] + E[v_1(N)|y^{N-1}] = \\
&= AE[x(N)|y^{N-1}] = A\tilde{x}(N|N-1)
\end{aligned} \tag{3.11}$$

where $E[v_1(N)|y^{N-1}] = 0$ since v_1 has zero mean value and is independent of y^N.

Since $E[x(t)] = E[e(t)] = 0, \; \forall t$, then:

$$E[x(N+1)|e(N)] = \Sigma_{x(N+1)e(N)}\Sigma^{-1}_{e(N)e(N)}e(N) = K(N)e(N) \tag{3.12}$$

where it can be proven that:

$$\begin{aligned}
&\Sigma_{x(N+1)e(N)} = AP(N)C^T \\
&\Sigma_{e(N)e(N)} = CP(N)C^T + V_2 \\
&K(N) = \Sigma_{x(N+1)e(N)}\Sigma^{-1}_{e(N)e(N)} = AP(N)C^T[CP(N)C^T + V_2]^{-1} \\
&P(N) = Var[\tilde{x}(N)] = E[\tilde{x}(N)\tilde{x}(N)^T]
\end{aligned}$$

The recursive form of the one-step state prediction is then:

$$\hat{x}(N+1|N) = A\hat{x}(N|N-1) + K(N)e(N) \tag{3.13}$$

where $K(N) \in \mathbb{R}^{n \times q}$ is called **one-step Kalman predictor gain matrix** and involves the prediction error variance $P(N) \in \mathbb{R}^{n \times n}$ of the state $x(N)$.

The prediction error variance $P(N) \in \mathbb{R}^{n \times n}$ of the state $x(N)$ can be recursively computed using the Difference Riccati Equation (DRE) which can be written as:

$$P(N+1) = AP(N)A^T + V_1 - K(N)[CP(N)C^T + V_2]K(N)^T \tag{3.14}$$

assuming $P(1) = Var[x(1)] = P_1$ as starting value.

The update of the state equation (3.13) has to be initialized as a starting value:

$$\hat{x}(1|0) = E[x(1)] = 0$$

The optimal estimate for the output $y(N+1)$ based on data y^N is given by:

$$\begin{aligned} \hat{y}(N+1|N) = E[y(N+1)|y^N] &= E[Cx(N+1) + v_2(N+1)|y^N] = \\ &= E[Cx(N+1)|y^N] + E[v_2(N+1)|y^N] = \\ &= CE[x(N+1)|y^N] + E[v_2(N+1)] = C\hat{x}(N+1|N) \end{aligned} \tag{3.15}$$

A graphical representation of the one-step Kalman predictor is shown in figure 3.3.

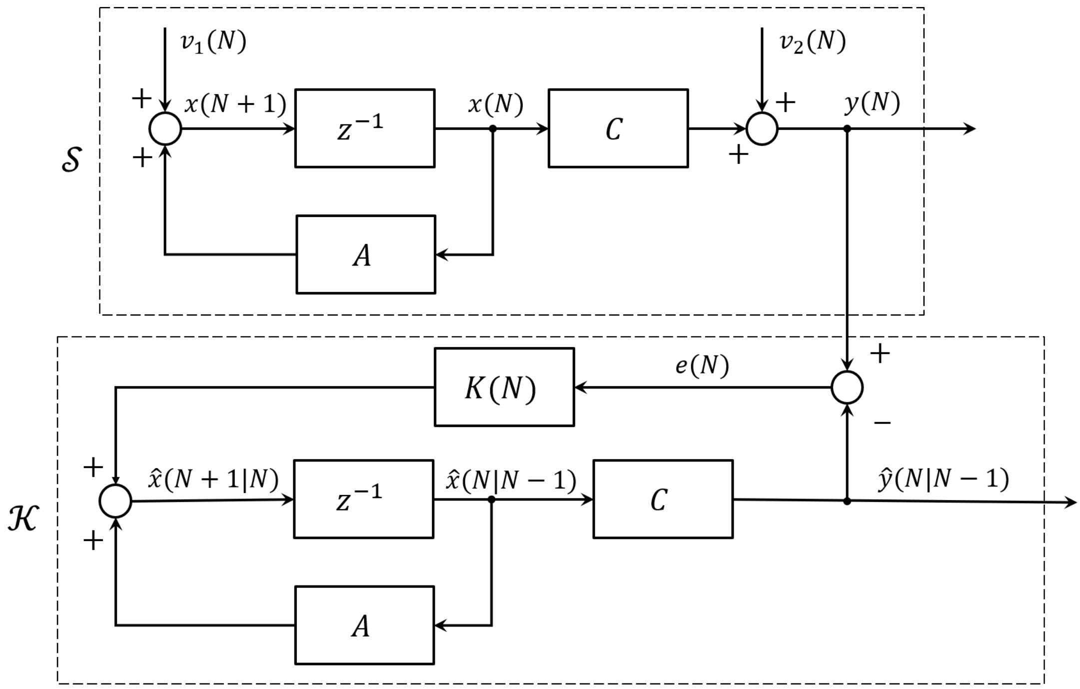

Figure 3.3: Graphical representation of the one-step Kalman predictor

3.1.3 Kalman filter

Let us consider a discrete-time, linear time-invariant (LTI), dynamical system $\mathcal{S}$ with an *exogeneous* (deterministic and known) input $u(\cdot)$ described by the state-space model:

$$\mathcal{S}\begin{cases} x(t+1) = Ax(t) + Bu(t) + v_1(t) \\ y(t) = Cx(t) + v_2(t) \end{cases} \qquad t = 1{,}2, ...$$

where $x(t) \in \mathbb{R}^n,\ y(t) \in \mathbb{R}^q,\ u(t) \in \mathbb{R}^p,\ v_1(t) \in \mathbb{R}^n,\ v_2(t) \in \mathbb{R}^q$, and assume that:

- $u(\cdot)$ may possibly depend on the output $y(\cdot)$ through a casual feedback as

$$u(t) = f(y(t), y(t-1), y(t-2), ...), \quad \forall t$$

- $v_1(t),\ v_2(t)$ are white noises with zero mean value that are correlated if considered at the same time but uncorrelated at different time instants:

$$E[v_i(t_1)v_j(t_2)^T] = V_{ij}\delta(t_2 - t_1), \quad i = 1{,}2, \quad j = 1{,}2$$

- $A \in \mathbb{R}^{n\times n},\ B \in \mathbb{R}^{n\times p},\ C \in \mathbb{R}^{q\times n},\ V_1 \in \mathbb{R}^{n\times n},\ V_2 \in \mathbb{R}^{q\times q},\ V_{12} \in \mathbb{R}^{n\times q}$ are known matrices
- the initial state $x(t=1)$ is an unknown random vector: $x(t=1) \sim (\bar{x}_1, P_1)$, with known $\bar{x}_1 \in \mathbb{R}^n$ and $P_1 \in \mathbb{R}^{n\times n}$, which is uncorrelated with $v_1(t), v_2(t)$
- the output measurements $y(t)$ are available for $t = 1{,}2, ..., N$

The optimal estimate for the state $x(N)$ based on data y^N is given by:

$$\hat{x}(N|N) = E[x(N)|y^N] = E[x(N)|y^{N-1}, y(N)] \tag{3.16}$$

where $y^{N-1} = [y(N-1)^T\ y(N-2)^T\ ...\ y(1)^T]^T \in \mathbb{R}^{(N-1)}q$.

From the Bayesian estimate formula, it results that:

$$\begin{aligned}\hat{x}(N|N) = E[x(N)|y^{N-1}, y(N)] = E[x(N)|y^{N-1}] + E[x(N)|e(N)] = \\ = \hat{x}(N|N-1) + E[x(N)|e(N)]\end{aligned} \tag{3.17}$$

where $e = (N) = y(N) - y(N-1)$ is the innovation if $y(N)$ given y^{N-1}.

Since $E[x(t)] = E[e(t)] = 0,\ \forall t$, then:

$$E[x(N)|e(N)] = \Sigma_{x(N)e(N)}\Sigma^{-1}_{e(N)e(N)}e(N) = K_0(N)e(N) \tag{3.18}$$

where it can be proved that:

$$\begin{aligned}&\Sigma_{x(N)e(N)} = P(N)C^T \\ &\Sigma_{e(N)e(N)} = CP(N)C^T + V_2 \\ &K_0 = \Sigma_{x(N)e(N)}\Sigma^{-1}_{e(N)e(N)} = P(N)C^T[CP(N)C^T + V_2]^{-1} \\ &P(N) = Var[\tilde{x}(N)] = E[\tilde{x}(N)\tilde{x}(N)^T]\end{aligned}$$

The optimal estimate for the state $x(t)$ based on data y^N can be obtained from the one-step Kalman predictor as:

$$\hat{x}(N|N) = \hat{x}(N|N-1) + K_0(N)e(N) \tag{3.19}$$

where $K_0 \in \mathbb{R}^{n \times q}$ is called **Kalman filter gain matrix** and involves the variance $P(N) \in \mathbb{R}^{n \times n}$ of $\tilde{x}(N)$. Note that, if $V_{12} = 0_{n \times q}$, then $K(N) = AK_0(N)$.

The variance of the filtering error $x(N) - \hat{x}(N|N)$ involves covariance $P(N)$ as well, since it can be proven that:

$$Var[x(N) - \hat{x}(N|N)] = P(N) - P(N)C^T[CP(N)C^T + V_2]^{-1}CP(N)$$
$$\Downarrow$$
$$Var[x(N) - \hat{x}(N|N)] \leq P(N)$$

since the estimate $\hat{x}(N|N)$ provided by the Kalman filter is based also on the data sample $y(N)$ with respect to the estimate $\hat{x}(N|N-1)$ provided by the one-step Kalman predictor. This means that the uncertainty on $\hat{x}(N|N)$ has to be lower.

The overall equations of the Kalman filter are:

$$\mathcal{K} : \begin{cases} \hat{x}(N+1|N) = A\hat{x}(N|N-1) + Bu(N) + K(N)e(N) \\ \hat{y}(N|N-1) = C\hat{x}(N|N-1) \\ \hat{x}(N|N) = \hat{x}(N|N-1) + K_0(N)e(N) \\ e(N) = y(N) - \hat{y}(N|N-1) \\ K_0(N) = P(N)C^T[CP(N)C^T + V_2(N)]^{-1} \\ K(N) = [AP(N)C^T[CP(N)C^T + V_{12}][CP(N)C^T + V_2(N)]^{-1} \\ P(N+1) = AP(N)A^T + V_1(N) - K(N)[CP(N)C^T + V_2(N)]K(N)^T \end{cases} \tag{3.20}$$

A graphical representation of the Kalman filter is given in figure 3.4

3.1.4 Extended Kalman Filter

Although Kalman filtering techniques by assumption can only be used on linear system, they can also be adapted to work with non-linear system. The Extended Kalman Filter (EKF) is one of these methods, based on the recursive linearization of the system around the current estimation state, then solving it as a linear estimation problem.

Let us consider a discrete-time, non-linear, time-variant, dynamic system $\mathcal{S}$ described by:

$$\mathcal{S} : \begin{cases} x(t+1) = f(t, x(t), u(t)) + v_1(t) \\ y(t) = h(t, x(t), u(t))) + v_2(t) \end{cases} \quad t = 1,2, ... \tag{3.21}$$

where $x(t) \in \mathbb{R}^n,\ y(t) \in \mathbb{R}^q,\ u(t) \in \mathbb{R}^p,\ v_1(t) \in \mathbb{R}^n,\ v_2(t) \in \mathbb{R}^q$, and assume that:

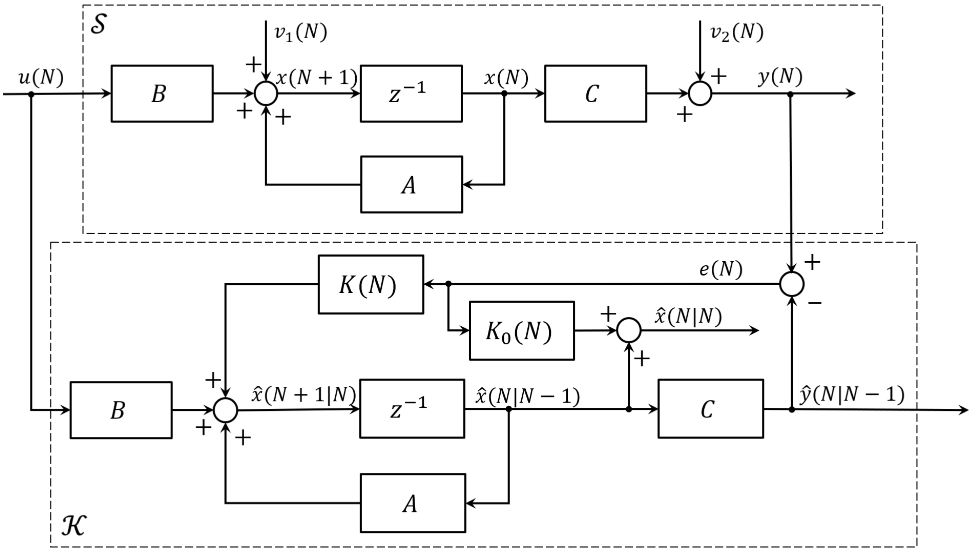

Figure 3.4: Graphical representation of the Kalman filter $\mathcal{K}$

- $v_1(t)$ and $v_2(t)$, respectively the process noise and the measurement noise, are white noises with zero mean value uncorrelated with each other and also with the initial state $x(1)$

- $f(\cdot)$ and $h(\cdot)$ are known nonlinear functions

- $V_1 \in \mathbb{R}^{n\times n}$ and $V_2 \in \mathbb{R}^{q\times q}$ are known matrices

- the initial state $x(t=1)$ is a random vector $x(t=1) \sim (\bar{x}_1, P_1)$ with known $\bar{x}_1 \in \mathbb{R}^n$ and $P_1 \in \mathbb{R}^{n\times n}$

- the output measurements $y(t)$ are available for $t = 1,2,...$

The matrices V_1, V_2 can be used as tuning parameters for the filter to achieve the desired performance: as the model error covariance matrix V_1 increases with respect to the measurement covariance matrix V_2, the filter tends trust the measurements more. On the contrary, if V_2 increases with respect to V_1, the filter tends to trust the model more, but the noise removal effect due to the V_1 matrix is reduced. The covariance matrices V_1 and V_2 represent the uncertainty assigned to either the model or the measurements.

The Extended Kalman filter is developed in the following two steps [17]:

1. **Prediction step**: the estimate $\hat{x}(N-1|N-1)$ of the state $x(N-1)$ obtained at the previous time step is combined with the current inputs to obtain the prediction of the next state $\hat{x}(N+1|N)$

2. **Correction step**: the predicted state $\hat{x}(N+1|N)$ is updated using the innovation term, that is the difference between measurements and the estimated model output.

Prediction step

The state equation is described by:

$$x(N+1) = f((x(N), u(N), N) + v_1(N) \tag{3.22}$$

Supposing that an estimate at time $N-1$ is available, equation (3.22) is expanded as a Taylor series around $\hat{x}(N-1|N-1)$, obtaining a linearized state equation:

$$\begin{aligned} x(N|N-1) \approx f(&\hat{x}(N-1|N-1), u(N), N)+ \\ &+ \frac{\partial f_x}{\partial x}|_{x=\hat{x}(N-1)}[x(N-1) - \hat{x}(N-1|N-1)] + v_1(N) \end{aligned} \tag{3.23}$$

By defining the one-step state prediction as:

$$\hat{x}(N|N-1) = f(\hat{x}(N-1|N-1), u(N), N) \tag{3.24}$$

and denoting with F the Jacobian matrix

$$F(N) = \nabla_x f_x(N) = \frac{\partial f_x(N)}{\partial x}|_{x=\hat{x}_{N-1}} \tag{3.25}$$

equation (3.22) can be written as a linear equation:

$$x(N+1) = F(N)x(N) + u(N) + v_1(N) \tag{3.26}$$

The state prediction error $\tilde{x}(N)$ and the prediction covariance matrix can be calculated:

$$\tilde{x}(N) = x(N) - \hat{x}(N|N-1) = F(N)\hat{x}(N-1|N-1) + v_1(N) \tag{3.27}$$

$$P(N|N-1) = F(N)P(N-1|N-1)F^T(N) + V_1(N) \tag{3.28}$$

The output equation in (3.21) can also be expanded using Taylor series, in order to obtain the predicted output vector $\hat{y}(N)$ and the innovation $e(N) = y(N) - h(\hat{x}(N|N-1))$. The Jacobian matrix of h is denoted with H and computed in $\hat{x}(N|N-1)$.

The linearized output equation becomes:

$$y(N) = H(N)x(N) + v_2(N) \tag{3.29}$$

while the innovation covariance matrix $S(N)$ is:

$$S(N) = H(N)P(N)H^T + V_2(N) \tag{3.30}$$

Correction step

Once the one-step prediction state is obtained, it is updated using the measurement vector $y(N)$. The corrected state is expressed as:

$$\begin{aligned}\hat{x}(N|N) = \hat{x}(N|N-1) + K(N)(y(N) - h(\hat{x}(N|N-1)) = \\ = \hat{x}(N|N-1) + K(N)e(N)\end{aligned} \quad (3.31)$$

where $K(N)$ is the Kalman gain matrix calculated to minimize the state error $\tilde{x}(N|N) = \hat{x}(N|N) - x(N)$. This can be done by minimizing the estimate covariance matrix $P(N|N)$ because the problems are equivalent [8].

$$\begin{aligned}P(N|N) = E[\tilde{x}(N)\tilde{x}(N)^T|y^N] \approx \\ \approx [I - K(N)H(N)]P(N|N-1)[I - K(N)H(N)]^T + K(N)V_2(N)K(N)\end{aligned} \quad (3.32)$$

By imposing the derivative of $P(N|N)$ equal to zero, the Kalman gain matrix is obtained:

$$K(N) = P(N|N-1)H(N)^T S(N)^{-1} \quad (3.33)$$

The overall equations of the Extended Kalman filter are:

- Prediction step

$$\begin{cases}\hat{x}(N|N-1) = f(\hat{x}(N-1|N-1), u(N), N) \\ P(N|N-1) = F(N)P(N-1|N-1)F(N)^T + V_1\end{cases} \quad (3.34)$$

- Correction step

$$\begin{cases}e(N) = y(N) - h(\hat{x}(N|N-1)) \\ S(N) = H(N)P(N|N-1)H(N)^T + V_2(N) \\ K(N) = P(N|N-1)H(N)^T S(N)^{-1} \\ \hat{x}(N|N) = \hat{x}(N|N-1) + K(N)e(N) \\ P(N|N) = (I - K(N)H(N))P(N|N-1)\end{cases} \quad (3.35)$$

3.2 Linear Matrix Inequalities

Another estimation technique has been used as a part of the vehicle dynamics estimator to estimate the wheel steering angle δ: the Linear Matrix Inequalities (LMIs) method.

LMIs are convex or quasi-convex constraints describing many optimization problems used in system and control theory. A linear matrix inequality has the form:

$$F(x) \triangleq F_0 + \sum_{i=1}^{m} x_i F_i > 0 \quad (3.36)$$

where $x \in \mathbb{R}^m$ is the variable and the symmetric matrices $F_i = F_i^T \in \mathbb{R}^{n\times n}$ for $i = 0,1,...,m$ are given.

The principle behind this observer is to estimate the state and the unknown input using the available measurements. The following assumptions must also be made:

- the number of unknown inputs shall be lower than the number of available measurements,
- the unknown inputs shall not be related to the measures,
- the considered model shall be observable.

LMIs can be used to represent a wide variety of constraints on x, like Lyapunov and convex quadratic inequalities [18]. Considering the following set of non-linear inequalities:

$$\begin{aligned} &R(x) > 0 \\ &Q(x) - S(x)R(x)^{-1}S(x)^T > 0 \end{aligned} \tag{3.37}$$

can be represented as a linear matrix inequality by applying Shur complement:

$$\begin{bmatrix} Q(x) & S(x) \\ S(x)^T & R(x) \end{bmatrix} > 0 \tag{3.38}$$

where $Q(x)$ and $R(x)$ are symmetrical matrices: $Q(x) = Q(x)^T,\ R(x) = R(x)^T$.

A typical problem that can be solved with LMIs is the Lyapunov inequality:

$$P > 0, \quad A^T P + PA < 0 \tag{3.39}$$

where $A \in \mathbb{R}^{n\times n}$ is known. In this case, the LMI is considered solved if the matrix P is found or if it is determined that no such P exists [18].

Chapter 4

Modular vehicle dynamics estimator

This chapters presents the structure of the proposed modular vehicle dynamics estimator and explains in detail the composition of each module and its role in the final structure.

The high level structure of the estimator is shown in figure 4.1, where the variables shown on the left side are the measurements used as inputs and the ones shown on the right side are the obtained estimates.

Figure 4.1 is presented as an array of blocks with different function to highlight the modular concept of the estimator, which has been one of the driving ideas during its development: the EKF is the "core" around which the other blocks have been added in order to increase the final performance of the estimator by introducing additional inputs or models.

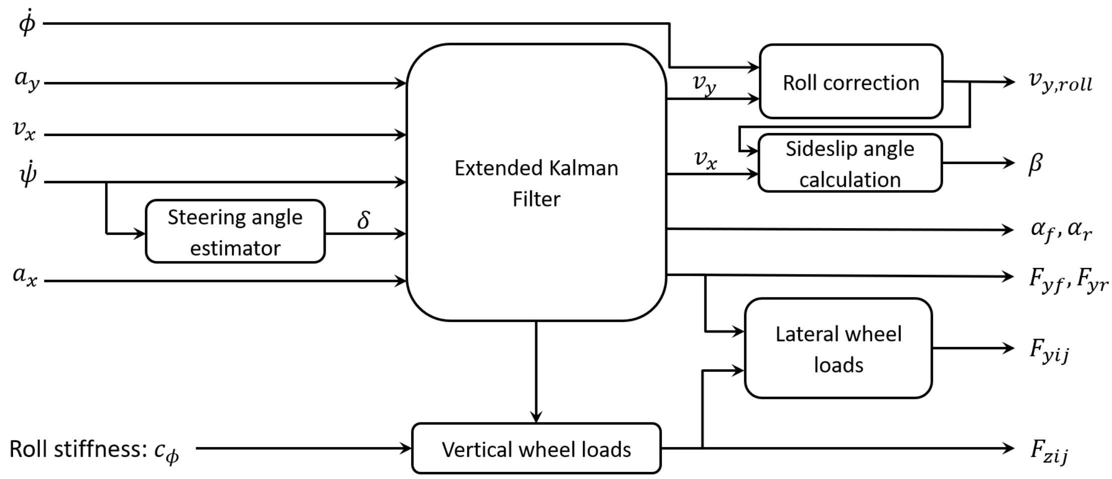

Figure 4.1: Modular vehicle dynamics estimator high-level structure

4.1 Extended Kalman Filter

The core of the vehicle dynamics modular estimator proposed in this thesis work is an Extended Kalman filter. Although the EKF is not an optimal solver for non-linear models, it has been chosen over other estimation techniques because of it has a low computational load, since it only considers the data obtained at the previous time step instead of the whole data history, making it suitable for real-time applications [19].

The EKF is based on the single-track model presented in section 2.3, resulting in the following model for the estimator:

$$\begin{cases} \dot{v_y} = \dfrac{-2(C_f + C_r)}{m \cdot v_x} v_y - \left(\dfrac{2(C_f \cdot l_f - C_r \cdot l_r)}{m \cdot v_x} + v_x \right) \dot{\psi} + \dfrac{2 \cdot C_f}{m} \delta \\ \ddot{\psi} = \dfrac{-2(C_f \cdot l_f - C_r \cdot l_r)}{I_{zz} \cdot v_x} v_y - \dfrac{2(C_f \cdot l_f^2 + C_r \cdot l_r^2)}{I_{zz} \cdot v_x} \dot{\psi} + \dfrac{2 \cdot C_f \cdot l_f}{I_{zz}} \delta \\ \dot{v_x} = a_x + v_y \cdot \dot{\psi} \\ \dot{C_f} = 0 \\ \dot{C_r} = 0 \end{cases} \tag{4.1}$$

where $x = [v_y,\ \dot{\psi},\ v_x,\ C_f,\ C_r]^T$ is the state vector and $u = [a_x, \delta]^T$ is the input vector. The cornering stiffness values C_f, C_r are modeled with a random walk model according to the adaptive linear tire model presented in section 2.2 in order to consider the non-linear behavior that the tire is supposed to have at low levels of lateral acceleration.

The measurement model (or output equation) considered at first is:

$$\begin{cases} \dot{\psi} = \dot{\psi} \\ a_y = \dfrac{-2 \cdot (C_f + C_r)}{m \cdot v_x} v_y - \dfrac{2 \cdot (l_f \cdot C_f - l_r \cdot C_r)}{m \cdot v_x} \dot{\psi} + \dfrac{2 \cdot C_f}{m} \delta \\ v_x = v_x \end{cases} \tag{4.2}$$

where $y = [\dot{\psi},\ a_y,\ v_x]$ is the measurement (or output) vector.

An observability analysis for an EKF which employs models (4.1) and (4.2) has been performed by Naets et al. in [10], from which the following remarks can be obtained:

- when the slip angles α_f and α_r are zero, the cornering stiffnesses C_f and C_r are unobservable, irrespective of the measurements used
- when the slip angles α_f and α_r are not zero, at least the yaw rate and lateral acceleration measurements are needed to make the system observable.

The first remark implies that during straight driving the cornering stiffnesses are subject to random drifting since there is no information about lateral dynamics that can be used to observe C_f and C_r. This is an issue, since straight driving is one of the most common driving conditions of a vehicle.

To overcome this issue, Van Aalst et al. proposed the introduction of model that assumes linear tire behavior in order to obtain a virtual sideslip measurement β_{lin}:

$$\begin{cases} \dot{v}_{y\ lin} = \dfrac{-2 \cdot \left(\bar{C}_f + \bar{C}_r\right)}{m \cdot v_x} v_{y\ lin} - \left(\dfrac{2 \cdot \left(\bar{C}_f \cdot l_f - \bar{C}_r \cdot l_r\right)}{m \cdot v_x} + v_x\right) \dot{\psi}_{lin} + \dfrac{2 \cdot \bar{C}_f}{m} \delta \\ \ddot{\psi}_{lin} = \dfrac{-2 \cdot \left(\bar{C}_f \cdot l_f - \bar{C}_r \cdot l_r\right)}{I_{zz} \cdot v_x} v_{y\ lin} - \dfrac{2 \cdot \left(\bar{C}_f \cdot l_f^2 + \bar{C}_r \cdot l_r^2\right)}{I_{zz} \cdot v_x} \dot{\psi}_{lin} + \dfrac{2 \cdot \bar{C}_f \cdot l_f}{I_{zz}} \delta \end{cases} \tag{4.3}$$

where $u = [v_x, \delta]$ is the input vector, $\bar{C}_f$ and $\bar{C}_r$ are the front and rear cornering stiffnesses, assumed to be constant.

Measurement model (4.2) is then augmented by introducing a virtual sideslip angle measurement β_{lin}, obtained by integrating over time linear model (4.3), remembering that, under the small angle approximation, $\beta_{lin} = \frac{v_{y\ lin}}{v_x}$.

The augmented measurement model is:

$$\begin{cases} \dot{\psi} = \dot{\psi} \\ a_y = \dfrac{-2 \cdot (C_f + C_r)}{m \cdot v_x} v_y - \dfrac{2 \cdot (l_f \cdot C_f - l_r \cdot C_r)}{m \cdot v_x} \dot{\psi} + \dfrac{2 \cdot C_f}{m} \delta \\ v_x = v_x \\ \beta_{lin} = \dfrac{v_{y\ lin}}{v_x} \end{cases} \tag{4.4}$$

where $y = [\dot{\psi},\ a_y,\ v_x,\ \beta_{lin}]^T$ is the measurement vector.

The virtual sideslip measurement has been added also to introduce an additional reference for the lateral velocity, which is one of the most important quantities to be obtained for control or dynamics analysis purposes, but at the same time it is very challenging to measure, especially at low levels of lateral acceleration. The difference in accuracy between measurements performed at medium ($0.1g \div 0.5g$) or low ($< 0.1g$) levels of lateral acceleration is shown in figure 4.2 for two sinusoidal handling maneuvers at constant velocity. It is evident that the quality of the measure in figure 4.2b is much lower than the one in figure 4.2a, showing more noise and drifting.

It has to be noted that, since the plots in figure 4.2 have been obtained with confidential data, more detailed information cannot be provided, such as the Y axes values, the commercial vehicle used in the maneuvers or the speed at which they have been performed.

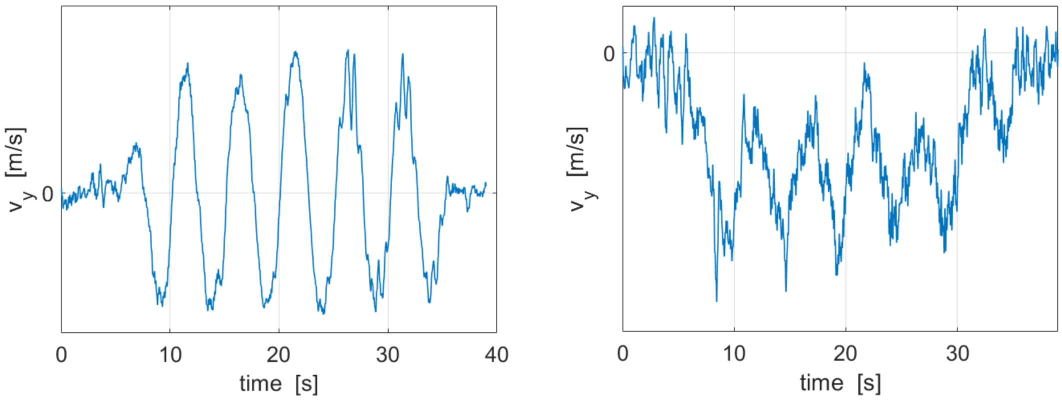

(a) v_y measured at medium levels of a_y (b) v_y measured at low levels of a_y

Figure 4.2: Sinusoidal maneuvers performed at different levels of lateral acceleration

By introducing the additional linear model, however, the β_{lin} reference obtained is the result of a model, simpler than the one used in equation (4.1), and not of an actual measure. This means that it is bound to have errors and limitations, but also moments in which its results correctly represent the actual behavior of the vehicle. For this reason, a measure of non-linearity s is defined, as a mean to determine whether the linear model 4.3 is reliable or not:

$$s(N) = |\dot{\psi}_{meas}(N) - \dot{\psi}_{lin}(N)| \tag{4.5}$$

where $\dot{\psi}_{meas}(N)$ and $\dot{\psi}_{lin}(N)$ are respectively the measured yaw rate and the yaw rate predicted by model (4.3) at time N.

This value is then used to adapt the covariances values of the adaptive linear tire model, Q_{C_f} and Q_{C_r}, and of the virtual sideslip angle measurement $R_{\beta_{lin}}$. The reasoning behind the adaptation of the covariances is the following:

- $\dot{\psi}_{meas} = \dot{\psi}_{lin} \rightarrow s = 0$: this occurs during straight driving, where no lateral excitation is present. In this case,
  - Q_{C_i} are set to zero to stabilize the estimator and avoid drifting of the cornering stiffnesses
  - $R_{\beta_{lin}}$ is set to a low value since the linear model is reliable in this condition
- $\dot{\psi}_{meas} \sim \dot{\psi}_{lin} \rightarrow s$ is small: the tire behavior is linear. In this case,
  - Q_{C_i} are set to low values since under linear behavior the cornering stiffnesses do not need to be adapted
  - $R_{\beta_{lin}}$ is set to a low value since β_{lin} is accurately predicts the vehicle behavior

- $\dot{\psi}_{meas} \neq \dot{\psi}_{lin} \rightarrow s$ is large: the tire behavior is non-linear. In this case,
  - Q_{C_i} are set to high values since the cornering stiffness values are not reliable in this condition and need to be adapted
  - $R_{\beta_{lin}}$ is set to a high value since β_{lin} is no longer an accurate estimate of the vehicle sideslip angle

The measure of non-linearity s is obtained by comparing the measured yaw rate with the one predicted from the linear model because the yaw rate is one of the most reliable quantities that are measured on a vehicle even in the challenging on-center condition, as it can be seen from figure 4.3.

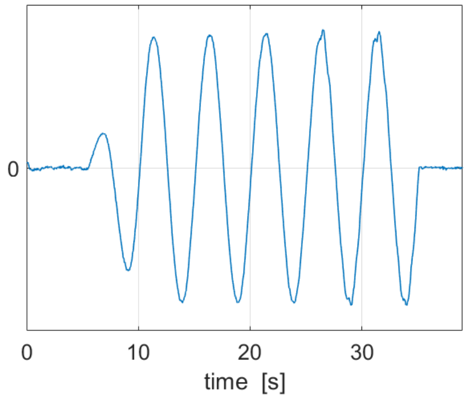

(a) $\dot{\psi}$ measured at medium levels of a_y

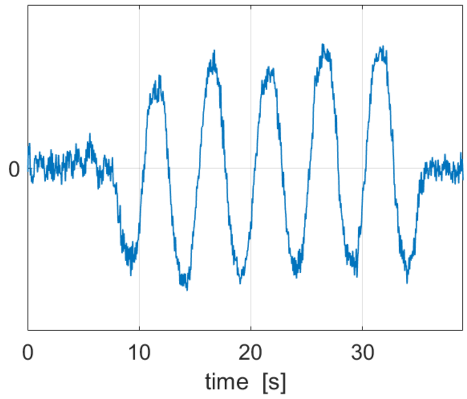

(b) $\dot{\psi}$ measured at low levels of a_y

Figure 4.3: Sinusoidal maneuvers performed at different levels of lateral acceleration

The quantities that are obtained as outputs of the estimator are the following:

- lateral velocity v_y
- longitudinal velocity v_x
- lateral acceleration a_y
- yaw rate $\dot{\psi}$
- front and rear cornering stiffnesses C_f and C_r
- front and rear tire slip angles α_f and α_r
- front and rear wheel lateral forces F_{yf} and F_{yr}

The tire slip angles are obtained by applying equations (2.11) and (2.12) to the system states and inputs, and the wheel lateral forces are obtained by combining the tire slip angles and the cornering stiffnesses, as in equation (2.2).

Figure 4.4 shows the final structure of the Extended Kalman Filter.

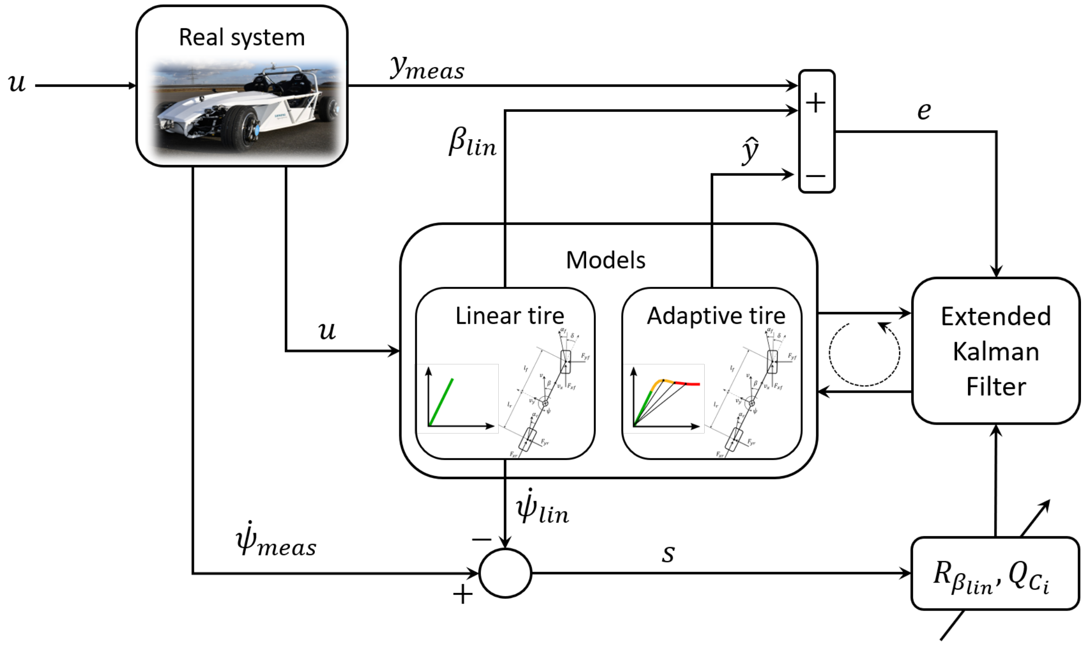

Figure 4.4: Extended Kalman Filter structure

4.1.1 Estimator tuning

The model covariance matrix Q is set as:

$$Q = \begin{bmatrix} Q_{v_y} & 0 & 0 & 0 & 0 \\ 0 & Q_{\dot{\psi}} & 0 & 0 & 0 \\ 0 & 0 & Q_{v_x} & 0 & 0 \\ 0 & 0 & 0 & Q_{C_f} & 0 \\ 0 & 0 & 0 & 0 & Q_{C_r} \end{bmatrix} \tag{4.6}$$

in which the covariances values are set as:

$$\begin{aligned} Q_{v_y} &= 0 \qquad (m/s)^2 \\ Q_{\dot{\psi}} &= 0 \qquad (rad/s)^2 \\ Q_{v_x} &= 1 \cdot 10^{-4} \cdot \Delta t \qquad (m/s)^2 \\ Q_{C_f} &= 1 \cdot 10^{-4} \cdot f_1(s) \cdot \Delta t \qquad (N/rad)^2 \\ Q_{C_r} &= 1 \cdot 10^{-4} \cdot f_1(s) \cdot \Delta t \qquad (N/rad)^2 \end{aligned}$$

where Δt is the time step between two consecutive measurements, and

$$f_1(s) = \begin{cases} 0, & \text{if } s \leq 0.015 \\ g(s) \cdot 500^2, & \text{otherwise} \end{cases} \tag{4.7}$$

in which $g(s)$ is a function that gives back the highest value of s in the last 1.5 seconds.

The measurement covariance matrix R is

$$R = \begin{bmatrix} R_{\dot{\psi}} & 0 & 0 & 0 \\ 0 & R_{a_y} & 0 & 0 \\ 0 & 0 & R_{v_x} & 0 \\ 0 & 0 & 0 & R_{\beta_{lin}} \end{bmatrix} \tag{4.8}$$

where the covariance values are obtained by computing the variance of the measured signals in the first 1.5 seconds of the maneuver (when the vehicle is still in straight driving conditions), resulting in:

$$\begin{aligned} R_{\dot{\psi}} &= 2 \cdot 10^{-6} \qquad (rad/s)^2 \\ R_{a_y} &= 1.5 \cdot 10^{-4} \qquad (m/s^2)^2 \\ R_{v_x} &= 7.8 \cdot 10^{-5} \qquad (m/s)^2 \\ R_{\beta_{lin}} &= f_2(s) \qquad (rad)^2 \end{aligned}$$

where

$$f_2(s) = \begin{cases} 10^{-7}, & \text{if } s \leq 0.015 \\ 1 \cdot 10^{-2} \cdot (2 \cdot g(s))^4, & \text{otherwise} \end{cases} \tag{4.9}$$

4.2 Wheel steering angle estimator

As mentioned in the previous section, one of the inputs of the models used in the EKF is the steering angle δ. However, it is not a measurement that is usually obtained with normal test equipment, as it requires expensive dedicated sensors placed on the wheel or suspension.

To overcome this issue, the wheel steering angle estimator developed by Giuseppe Streppa in a preceding thesis work at Siemens [11] has been introduced as a means to obtain δ starting from the available measured data, using a linear matrix inequalities method.

The model used is again the single-track one:

$$\begin{cases} \dot{\beta} = \dfrac{F_{yf} + F_{yr}}{v_{CoG} \cdot m} - \dot{\psi} \\ \\ \ddot{\psi} = \dfrac{l_f \cdot F_{yf} - l_r \cdot F_{yr}}{I_{zz}} \end{cases} \tag{4.10}$$

where equation (4.10) can be rewritten as a linear system Σ with unknown input δ.

$$\Sigma : \begin{cases} \dot{x} = Ax + B\delta \\ y = Cx \end{cases} \tag{4.11}$$

in which $x = [\beta,\ \dot{\psi}]^T$ is the state vector, δ is the unknown input and $y = \dot{\psi}$ is the output vector. Using the small angle approximation, and remembering that the lateral forces are proportional to the tire slip angles (2.1), the matrices A, B, C can be expressed as:

$$A = \begin{bmatrix} \dfrac{-C_f - C_r}{m \cdot v_{CoG}} & \dfrac{l_r \cdot C_r - l_f \cdot C_f}{m \cdot v_{CoG}^2} \\[2ex] \dfrac{l_r \cdot C_r - l_f \cdot C_f}{I_{zz}} & \dfrac{-l_r^2 \cdot C_r - l_f^2 \cdot C_f}{I_{zz} \cdot v_{CoG}} \end{bmatrix}$$

$$B = \begin{bmatrix} \dfrac{C_f}{m \cdot v_{CoG}} \\[2ex] \dfrac{l_f \cdot C_f}{I_{zz}} \end{bmatrix}$$

$$C = \begin{bmatrix} 0 & 1 \end{bmatrix}$$

The state and the input of system Σ are estimated with an Unknown Input Observer (UIO) $\mathcal{O}$ (4.12):

$$\mathcal{O} : \begin{cases} \dot{z} = Nz + Ly \\ \hat{x} = z - Ey \end{cases} \tag{4.12}$$

where z is the state of the observer ans $\hat{x}$ is the output corresponding to the estimated variable. The matrices N, L and E have to be computed. The estimation error $e = x - \hat{x}$ converges asymptotically to 0 if and only if the following conditions are met:

1. N is stable
2. $PB = 0$
3. $LC = PA - NP$

where $P = I + EC$ and I is the identity matrix. The first condition can be transformed in a LMI using Lyapunov's theorem and Shur complement [11]:

$$\begin{bmatrix} -X & 0 \\ 0 & (PA)^T X + X(PA) - (C^T W^T + WC) \end{bmatrix} < 0 \tag{4.13}$$

where W is the matrix variable and X is the symmetric positive matrix variable, which are obtained by solving the LMI problem.

From the second and third conditions, the following equations are obtained:

$$\begin{aligned} &E = -B(CB)^T[(CB)(CB)^T]^{-1} \\ &N = PA - X^{-1}WC \\ &L = X^{-1}W(I + CE) - PAE \end{aligned} \tag{4.14}$$

Then, the unknown input observer system $\mathcal{O}$ (4.12) is solved, obtaining $\hat{x} = [\beta,\ \dot{\psi}]$. Finally, the steering angle δ is computed from Σ:

$$\delta = B^{+}(\dot{z} - E\dot{y} + A\hat{x}) \tag{4.15}$$

where B^{+} is the pseudo-inverse of B.

4.3 Roll correction

It has been observed that the lateral velocity v_y estimated by the extended Kalman filter has a phase difference with respect to the measured data, as shown in figure 4.5.

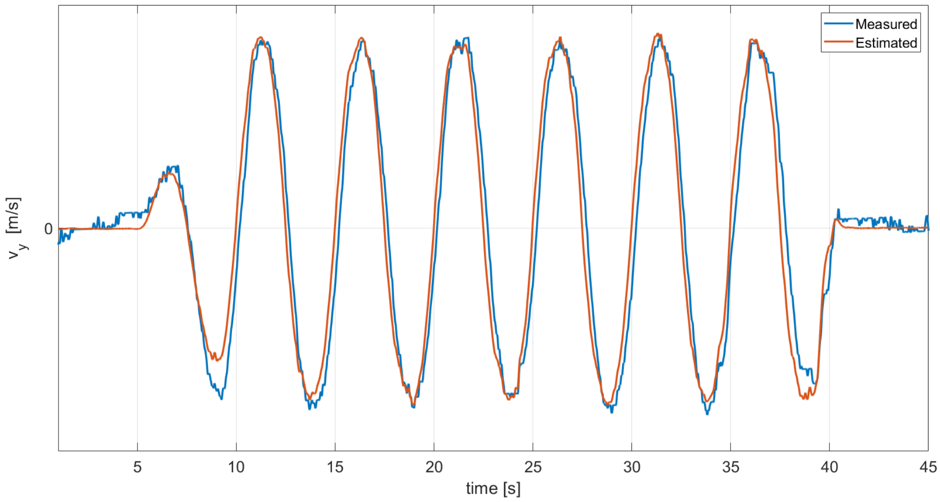

Figure 4.5: Comparison between measured and estimated lateral velocity

This error is thought to be due to the fact that the roll motion is neglected in the model used in the EKF. The roll angle ϕ causes the lateral acceleration to be influenced by an additive component that needs to be considered in the single-track model. According to simulations performed with AmeSim, the main contribution of roll is given by the roll rate $\dot{\phi}$, and to compensate for the phase mismatch a correction using this term is introduced by Ricci in [8]:

$$v_{y,roll} = v_y - \dot{\phi} \cdot h_r \tag{4.16}$$

where $v_{y,roll}$ is the corrected lateral velocity, v_y is the lateral velocity estimated by the EKF, $\dot{\phi}$ is the vehicle roll rate and h_r is the roll center height.

The results of the correction applied by (4.16) are shown in figure 4.6. The phase difference is almost completely removed, the remaining error is attributed to the roll acceleration $\ddot{\phi}$ which is neglected here. Introducing the roll rate measurement has also the effect of increasing the dynamic content of the estimated lateral velocity: by comparing figure 4.5 and 4.6, it is clear that the estimated lateral velocity shown in the latter follows more closely the dynamic content of the measured signal.

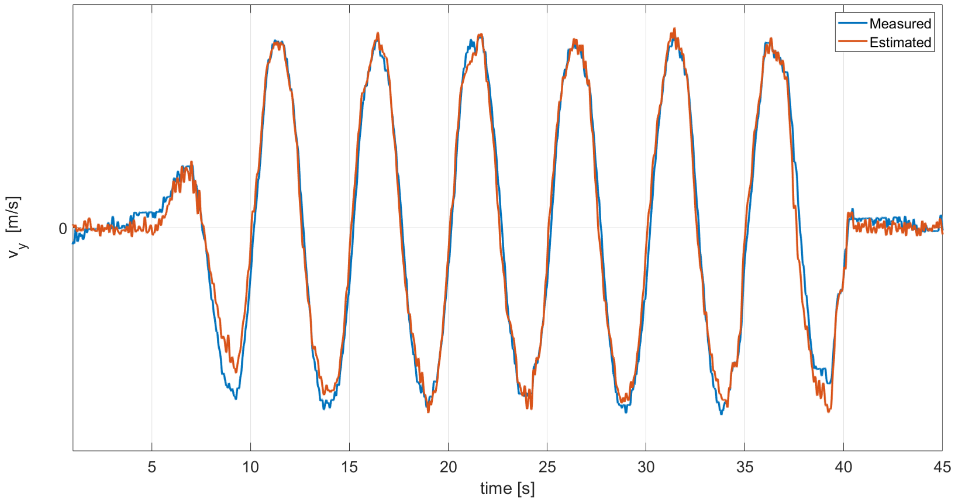

Figure 4.6: Estimated lateral velocity with roll correction

4.3.1 Sideslip angle calculation

The same phase mismatch noticed for the lateral velocity is observed also for the sideslip angle β (figure 4.7). This is expected, since β is related to v_y.

By using the corrected lateral velocity $v_{y,\ roll}$ to compute the sideslip angle value:

$$\beta_{roll} = \tan^{-1}\left(\frac{v_{y,\ roll}}{v_x}\right) \tag{4.17}$$

the phase mismatch is corrected (figure 4.8).

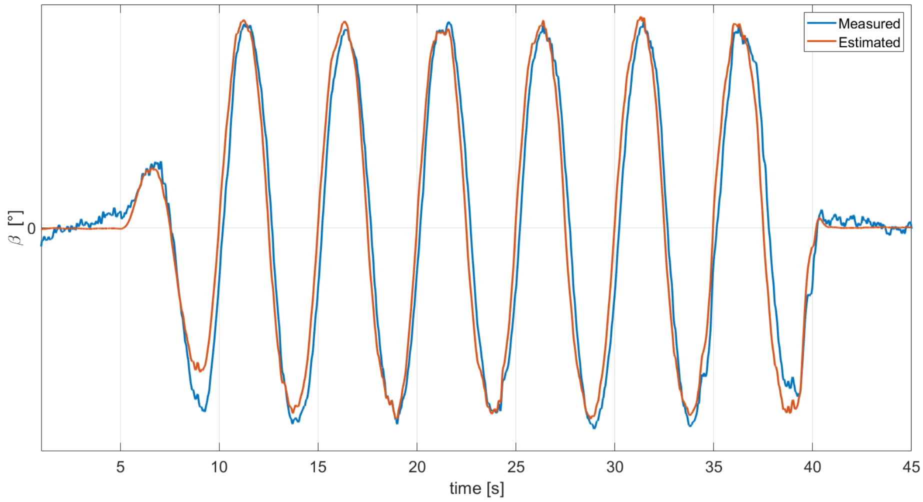

Figure 4.7: Measured and estimated sideslip angle β

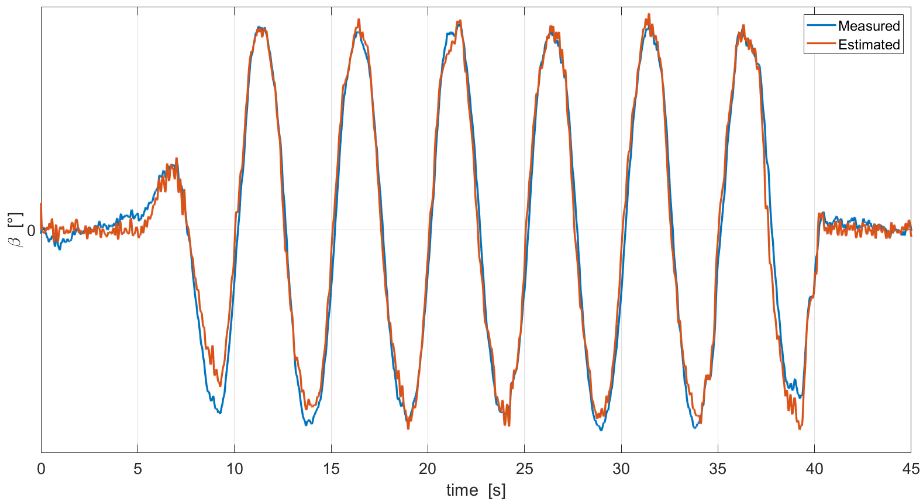

Figure 4.8: Estimated vehicle sideslip angle with roll correction

4.4 Vertical wheel loads

In section 4.3 it was shown that by introducing additional information such as the roll rate measurement $\dot{\phi}$ and the height of the roll center h_r, to the set of parameters and measurements already used in the EKF, the quality of the results is improved. In this section it is shown that by introducing the front and rear roll stiffnesses $c_{\phi f}$ and $c_{\phi r}$, access to the tire vertical forces is obtained [15].

By considering the two-track model explained in section 2.4, the longitudinal and lateral variations of the vertical loads are obtained with equations (2.14) and (2.15), and they are used to compute the vertical loads for each wheel:

$$\begin{aligned} F_{zfl} &= \frac{m \cdot g \cdot l_r}{2 \cdot WB} - \Delta F_{zyf} - \Delta F_{zx} \\ F_{zfr} &= \frac{m \cdot g \cdot l_r}{2 \cdot WB} + \Delta F_{zyf} - \Delta F_{zx} \\ F_{zrl} &= \frac{m \cdot g \cdot l_f}{2 \cdot WB} - \Delta F_{zyr} + \Delta F_{zx} \\ F_{zrr} &= \frac{m \cdot g \cdot l_f}{2 \cdot WB} + \Delta F_{zyr} + \Delta F_{zx} \end{aligned} \tag{4.18}$$

The roll stiffness parameters are obtained through Kinematic & Compliance (K & C) testing, which is a particular type of suspension testing focused on the suspension geometry (toe angle, camber angle, etc.) and stiffness.

The resulting estimated tire forces show a very close match both in amplitude and phase with the measurements obtained with force transducers and strain gauges, as shown in figure 4.9.

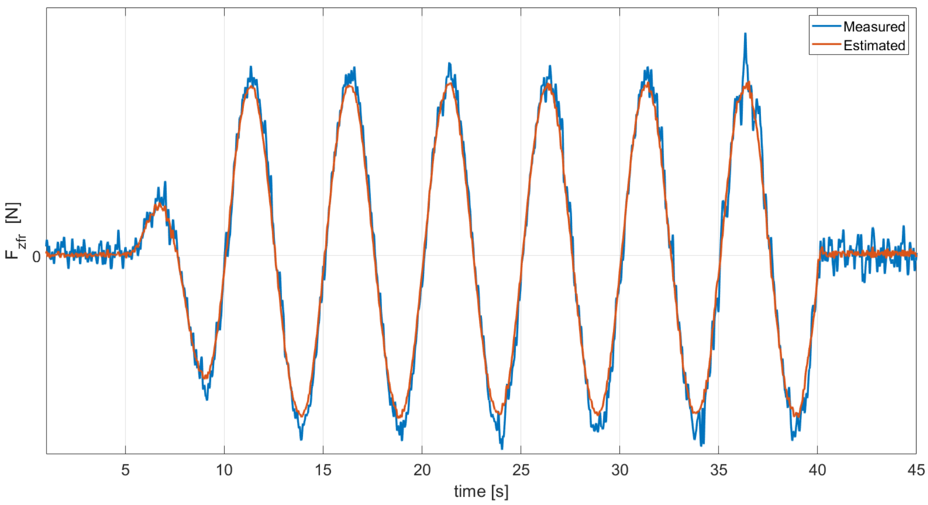

Figure 4.9: Measured and estimated vertical load on the front right wheel

4.5 Lateral wheel loads

Once the vertical wheel loads have been determined, the lateral wheel forces are obtained by applying the vertical proportionality principle, which states that the difference between the lateral forces on the left and right wheels is proportional to the weight distribution, assuming that the friction coefficient for the left and right wheel is the same. The lateral wheel forces can then be computed as [20]:

$$F_{yij} = F_{yi} \frac{F_{zij}}{F_{zi,left} + F_{zi,right}} \tag{4.19}$$

for $i \in \{front, rear\}$ and $j \in \{left, right\}$. An example of the estimated lateral force is shown in figure 4.10, where it is compared to the lateral force measured using strain gauges and force transducers.

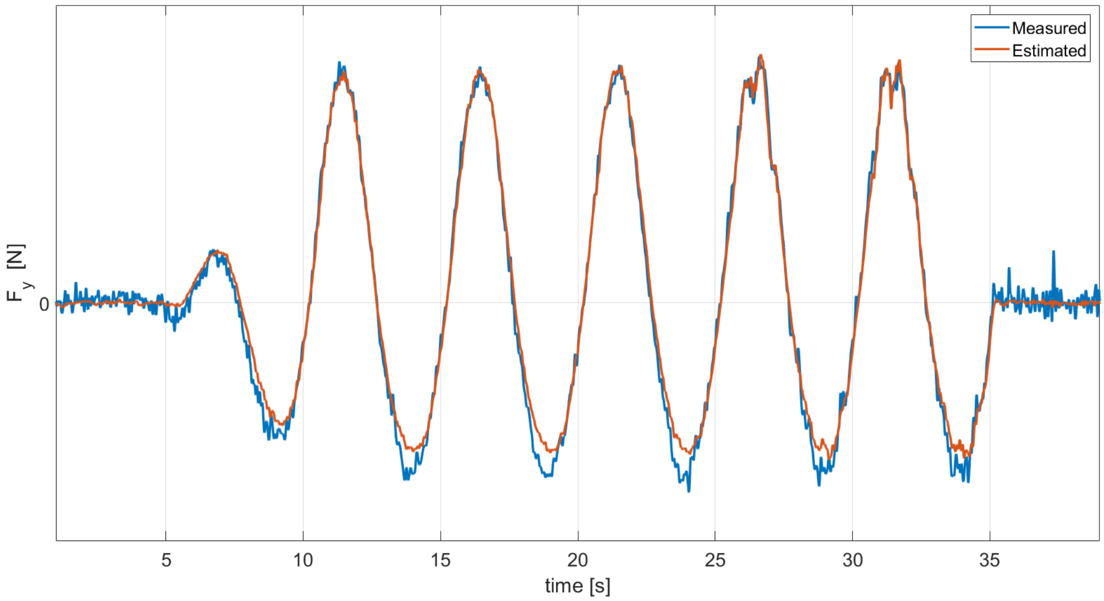

Figure 4.10: Measured and estimated lateral forces for the rear right wheel

The estimated curve is a close fit with respect to the measured one, and the small differences in amplitude are attributed to the neglected effects of ply-steer and tire conicity [12].

Chapter 5

Track tests

This chapter gives an overview of the sensors used for the measurements, their placement on the vehicle, the needed vehicle parameters and how they are obtained, and the driving maneuvers used for testing and validation of the estimator.

5.1 Sensors equipment

In order to obtain a large amount of measured data, various physical sensors have been employed in the testing campaign.

The sensor equipment used for testing is summarized in table 5.1.

Sensor type	**Manufacturer**	**Model**
Inertial Measurement Unit	OxTS	RT3003G
Optical sensor	Kistler	Correvit S-Motion
Strain gauges	Vishay, Micro-Measurements	125UN-350 062UV-350 062UT-350
Wheel motion measurement	Aicon	WheelWatch
Wheel force transducer	Kistler	RoaDyn (6 DOF)
LMS SCADAS	Siemens	Mobile 5

Table 5.1: Sensor equipment on test vehicles

The OxTS RT3003G [21] is an Inertial Navigation System for making precision measurements of motion in real-time. It is equipped with two GNSS antennas, three gyroscopes and three accelerometers. This IMU (shown in figure 5.1) is placed inside the vehicle, in a location close to the center of gravity, usually between the two front seats. It provides precise measurements for linear and angular displacements, velocities and accelerations along the X, Y and Z axes. The data it produces is used as a reference for the linear accelerations and velocities, as well as angular rates.

Figure 5.1: OxTs RT3003G Inertial Measurement Unit

The Correvit S-Motion (figure 5.2) is a non-contact optical sensor which enables direct, slip-free measurement of longitudinal and transverse speed in vehicle driving dynamics tests [22]. Out of the three vehicles used for the estimator validation, this sensor was mounted only on the SimRod (figure 5.8). It is placed in the nose of the vehicle, at equal distance from the two wheels, facing downward. It was used to obtain a more precise measure of the lateral and longitudinal velocities, as well as of the sideslip angle, since the ones produced by the IMU are a result of the integration of the linear accelerations and as such are prone to errors.

The Vishay Micro-Measurements strain gauges (figure 5.3) are used for load identification. A number of them is placed at determined positions on the suspension structure, and the information obtained from them is combined to compute the longitudinal, vertical and lateral loads on the wheel.

The Aicon WheelWatch system (figure 5.4) provides non-contact high speed monitoring of wheel motion in vehicle dynamics testing [23]. It provides accurate measurements of all wheel parameters including steering angle, camber inclination, slip angle, spring travel. It is built around a high-resolution high speed digital camera that frames the optical targets on the carbon fiber adaptor fixed to the wheel. Special optical targets applied to the fender define the vehicle coordinate system, so that WheelWatch can continuously recalculate its position. It has been mounted only on one of the two commercial vehicles used for the estimator validation, and it is used to validate the estimated tire slip angles.

The Kistler RoaDyn wheel force transducers (figure 5.5) have been used for direct measurement of the wheel forces. They measure operating loads and torques during typical vehicle driving maneuvers [24]. Four wheel force transducers, one per wheel, have been mounted on the vehicles as a means to obtain more precise

Figure 5.2: Kistler Correvit S-Motion

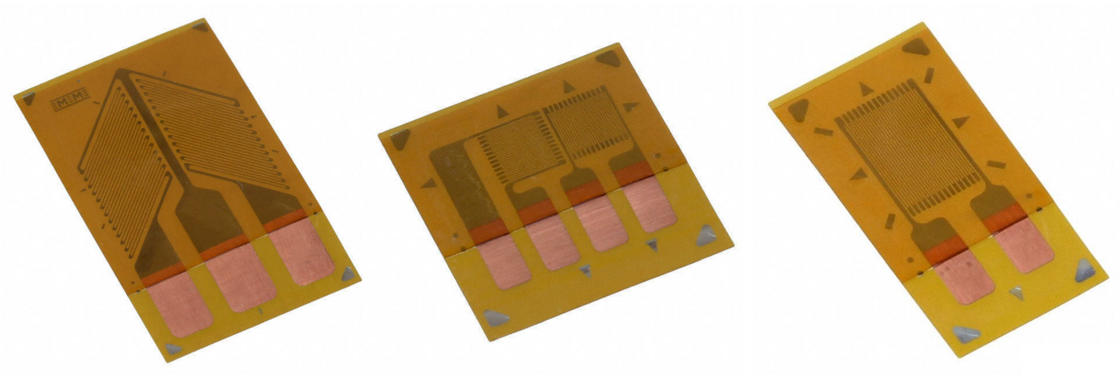

(a) 062UT-350 (b) 062UV-350 (c) 125UN-350

Figure 5.3: Strain gauges employed for load identification procedure

lateral force measurements.

The Siemens PLM SCADAS (figure 5.6) is a multi-channel data acquisition system used to interface with all the utilized sensors.

The position of the sensor equipment on the SimRod vehicle is shown in figure 5.7.

Figure 5.4: Aicon Wheel Watch system

Figure 5.5: Kistler RoaDyn wheel force transducer

Figure 5.6: Siemens PLM SCADAS Mobile

(a) SimRod sensors position, front view

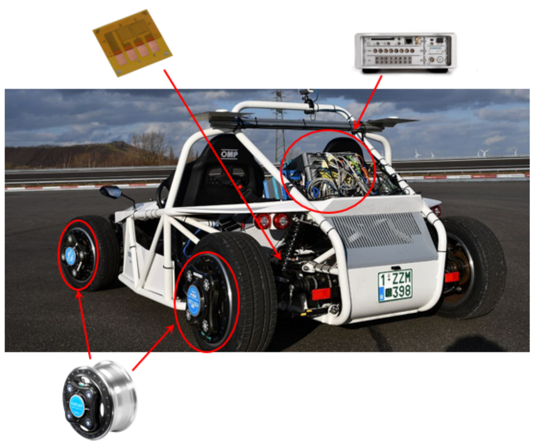

(b) SimRod sensors position, rear view

Figure 5.7: Placement of sensor equipment on the SimRod vehicle

5.2 Vehicle instrumentation

The vehicles used in the test campaign were three: two commercial vehicles, about which no information will be provided here due to its confidential nature, and the SimRod (figure 5.8).

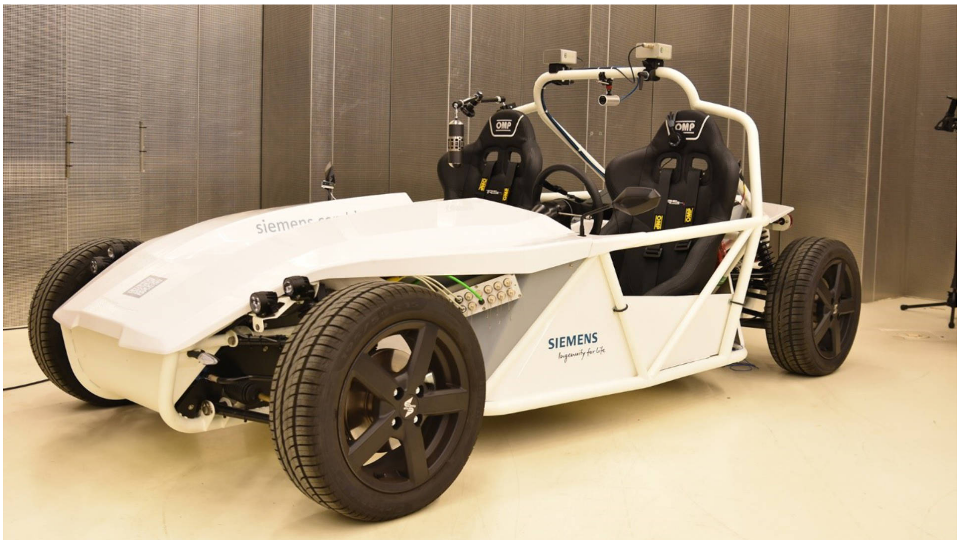

Figure 5.8: SimRod vehicle

The SimRod is an electric sports car developed by Siemens to be used as a technology demonstrator and testing device. Table 5.2 summarizes the vehicle parameters used in the estimator.

The wheelbase and track width values are obtained from the CAD model of the SimRod, while the mass has been measured with scales placed under each wheel.

The weight measurements for each axle have then been used to compute the longitudinal position of the center of gravity:

$$l_f = \frac{m \cdot g}{F_{zr} \cdot WB} \tag{5.1}$$

where m is the total mass of the vehicle, WB is the wheelbase and F_{zr} is the measured weight of the rear axle.

The CoG height has been measured using the wheel scale method proposed in [25]: after recording the wheel weights and the other parameters at normal trim, one end of the vehicle is elevated and the pitch angle θ and the front and rear axle weights F_{zf0} and F_{zr0} are measured (figure 5.9). The height of the center of gravity is then calculated:

$$h_{CoG} = \frac{F_{zf0} - m \cdot g(\frac{l_r}{WB})}{(\frac{m \cdot g}{WB})} + \frac{F_{zf0}(r_f - r_r)}{m \cdot g} + r_r \tag{5.2}$$

Parameter	Value	Unit
Mass (m)	930	kg
Yaw Inertia (I_{zz})	700	kg·m^2
Wheelbase (WB)	2.346	m
CoG distance from the front axle (l_f)	1.171	m
Track width (t)	1.402	m
Cornering stiffness, front axle (C_f)	2.8·10^4	N/rad
Cornering stiffness, rear axle (C_r)	5.2·10^4	N/rad
CoG height (h_{CoG})	0.19	m
Roll center height (h_r)	-	m
Roll stiffness, front axle ($c_{\phi f}$)	-	N/mm
Roll stiffness, rear axle ($c_{\phi r}$)	-	N/mm

Table 5.2: SimRod parameters

where r_f and r_r are respectively the front and rear wheel radii.

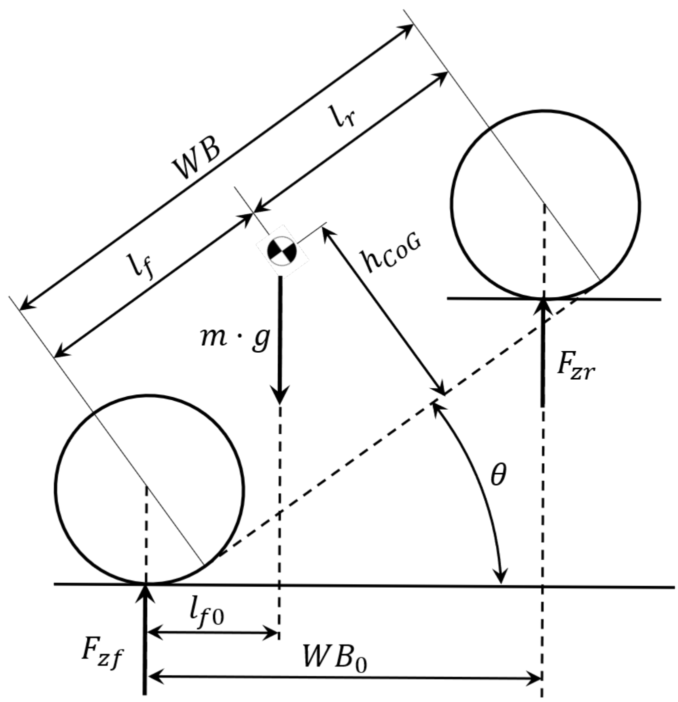

Figure 5.9: Graphical representation of the wheel scale method

The cornering stiffnesses values, needed as initial estimates that are then iteratively updated by the EKF, can be obtained with several approaches, such as [26]. In this case, a first estimate was obtained with the cited method and then it was tuned to obtain a better fit between estimated and measured data.

The yaw inertia has been estimated using the method proposed by Bixel in [27]:

$$I_{zz} = \frac{t \cdot WB}{K} m \tag{5.3}$$

where t is the track width and $K = 4.1942$ is an approximation constant dependent on inertia property and vehicle class. The resulting I_{zz} has an average error of almost 10%, but since variations of the yaw inertia of this entity do not cause observable changes in the estimator results, it was deemed acceptable.

The roll center height, as well as the front and rear roll stiffnesses, are obtained from K&C testing which has not been performed for the SimRod, so those spots are left blank in table 5.2.

5.3 Maneuvers description

Two different kind on maneuvers have been used in the testing campaign: sinusoidal maneuvers at constant velocity and step steer maneuvers at constant velocity.

The sinusoidal maneuvers are performed at different velocity in order to have data at both medium and low levels of lateral acceleration. These maneuvers have been used to verify the correct functioning of the estimator in all the conditions of interest. For the two commercial vehicles, a steering robot was used, while the SimRod was driven manually. Figure 5.10 shows the steering angles of one of the two commercial vehicles (figure 5.10a) and for the SimRod (figure 5.10b), where the difference between the vehicle driven with a steering robot and manually can be seen.

The second maneuver used was a step steer to the left, performed at different levels of velocity in order to have data at medium and low levels of lateral acceleration. The data obtained from the step steer maneuver has been used to observe the difference in the forces build-up on the base and modified version of the same vehicle. As already mentioned, the data for the two commercial vehicles has been obtained with a steering robot while the SimRod has been driven manually. Figure 5.11 shows the steering angles of one of the commercial vehicle and of the SimRod.

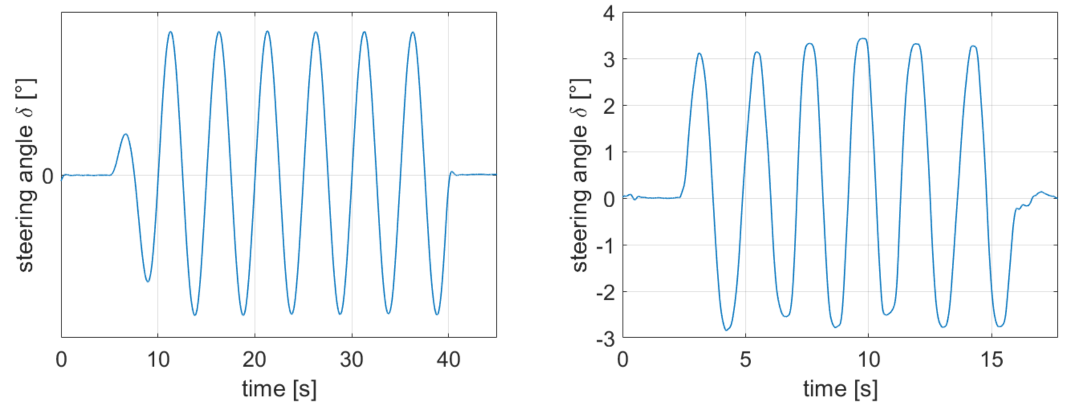

(a) Steering angle for a commercial vehicle (b) Steering angle for the SimRod vehicle

Figure 5.10: Sinusoidal maneuvers performed on different vehicles

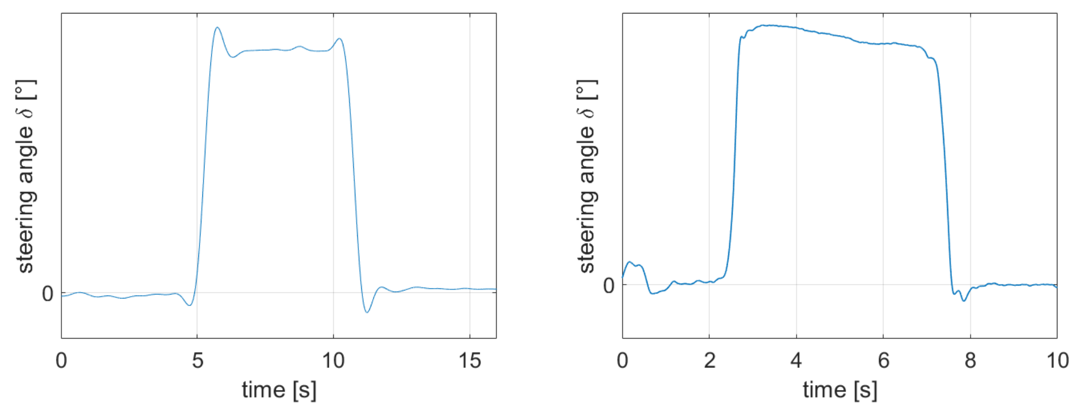

(a) Steering angle for a commercial vehicle (b) Steering angle for the SimRod vehicle

Figure 5.11: Step steer maneuvers performed on different vehicles

Chapter 6

Test validation

The validation of the modular vehicle dynamics estimator has been divided in four steps, which are treated in the following sections:

- section 6.1 shows the results of the estimation of the EKF states
- section 6.2 demonstrates that accurate estimation of additional quantities is achieved
- section 6.3 proves that the estimator enhances the quality of certain signals measured at boundary conditions
- section 6.4 provides a practical application of the estimator, where it is used to detect the expected differences in the base and modified version of the same vehicle.

6.1 State estimation

The EKF provides the estimation of the states $x = [v_y,\ \dot{\psi},\ v_x,\ C_f,\ C_r]^T$. Since the cornering stiffness as a parameter are not measured, the C_f and C_r resulting from the estimator cannot be compared to real data. They are, however, used to compute the other states and the lateral loads, so they are considered validated if the estimation of the other quantities is accurate. The data shown in this section has been obtained with a sinusoidal maneuver at constant velocity of around 60 km/h and lateral acceleration of around 0.35 g on the SimRod vehicle. The reported values of velocity and lateral acceleration are approximations since the vehicle has been driven manually without the help of steering or accelerating robots.

Lateral velocity

The lateral velocity v_y and its relative error are shown in figure 6.1, and the blue line in figure 6.1a is the data measured with the Correvit S-Motion sensor and the

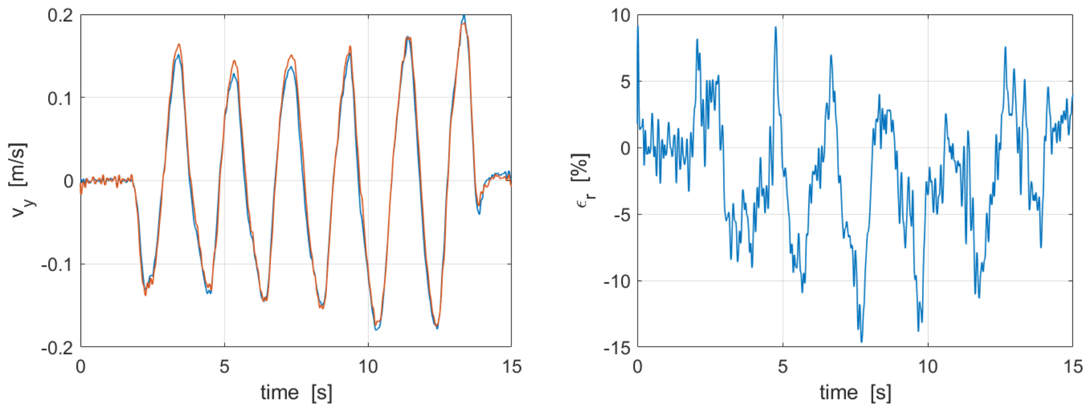

(a) Lateral velocity (b) Relative error of the estimated v_y

Figure 6.1: Lateral velocity and its relative error

orange one is the result of the estimator, with the roll correction applied; it can be seen that the two curves are almost entirely overlapped. This is an excellent result since it means that the estimator is able to reproduce with a good degree of precision the measurements taken with an high-grade optical sensor.

Yaw rate

Figure 6.2 shows the results for the yaw rate estimation and its relative error In

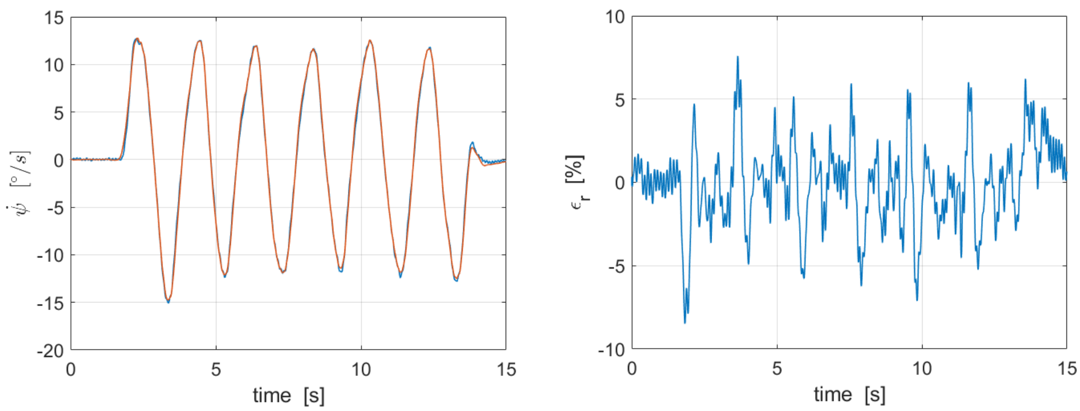

(a) Yaw rate (b) Relative error of the estimated $\dot{\psi}$

Figure 6.2: Yaw rate and its relative error

figure 6.2a the blue line is the quantity measured with the OxTS Inertial Measurement Unit (IMU) and the orange one is the estimated state $\dot{\psi}$. The two curves are almost indistinguishable between each other, as both the amplitude and the phase are reproduced correctly. This is to be expected, since the yaw rate is also one of the measures used as reference in the EKF. The orange curve can, in fact, be made to follow the behavior of the blue one more closely (or less) by modifying the relative covariance values, as explained in section 4.1.

Longitudinal velocity

The longitudinal velocity v_x and its relative error are shown in figure 6.3, where

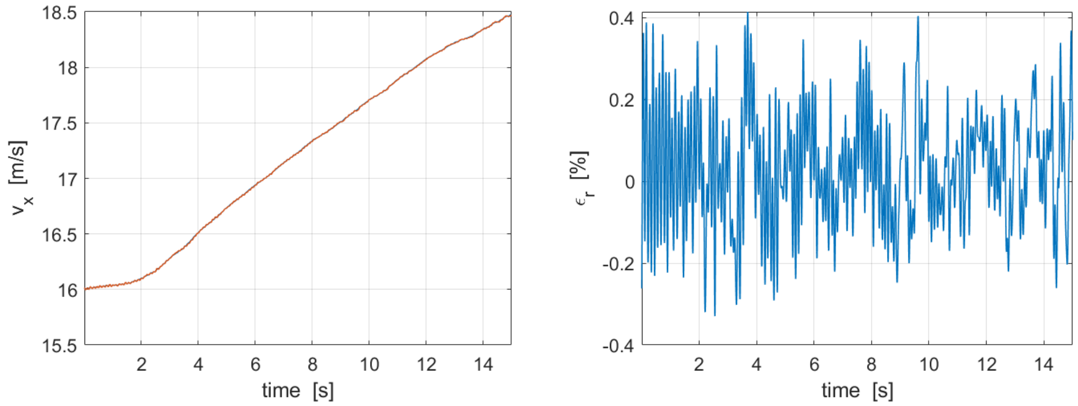

(a) Longitudinal velocity (b) Relative error of the estimated v_x

Figure 6.3: Longitudinal velocity and its relative error

in figure 6.3a the blue line is the velocity measured by the Correvit S-Motion sensor and the orange line is the corresponding estimated state. The two lines are completely overlapped, as the estimator perfectly reproduces the measured data. Again, this is to be expected as the same considerations made for the yaw rate also hold here, the longitudinal velocity being both a state and an output of the EKF.

6.2 Estimation of additional quantities

In this section, it is demonstrated how the estimator expands the amount of available signals: by taking as inputs or references the yaw rate, roll rate, longitudinal velocity and acceleration and lateral acceleration, all measured with an IMU, the following new quantities are estimated:

- Vehicle sideslip angle β
- Front and rear axle slip angles α_f and α_{fr}
- Front and rear axle lateral loads F_{yf} and F_{yr}
- Vertical wheel loads F_{zfl}, F_{zfr}, F_{zrl} and F_{zrr}
- Lateral wheel loads F_{yfl}, F_{yfr}, F_{yrl} and F_{yrr}

Vehicle sideslip angle

The vehicle sideslip angle β and its relative error for the SimRod are shown in figure 6.4. In figure 6.4a the blue line is the data measured with the Correvit S-Motion

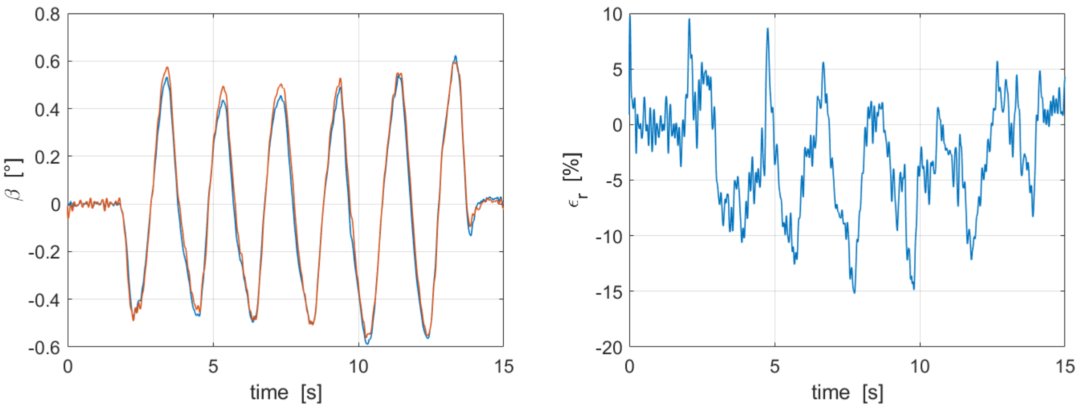

(a) Vehicle sideslip angle β (b) Relative error of the estimated β

Figure 6.4: Vehicle sideslip angle and its relative error

sensor and the orange line is the estimated sideslip angle. Both the amplitude and phase show a very close match, and the dynamics content of the measured signal is reproduced in the estimated one.

Front, rear tire slip angles

The tire slip angles for the front and rear axles α_f and α_r are shown in figure 6.5, where the blue lines are the data measured with the sensors and the orange lines

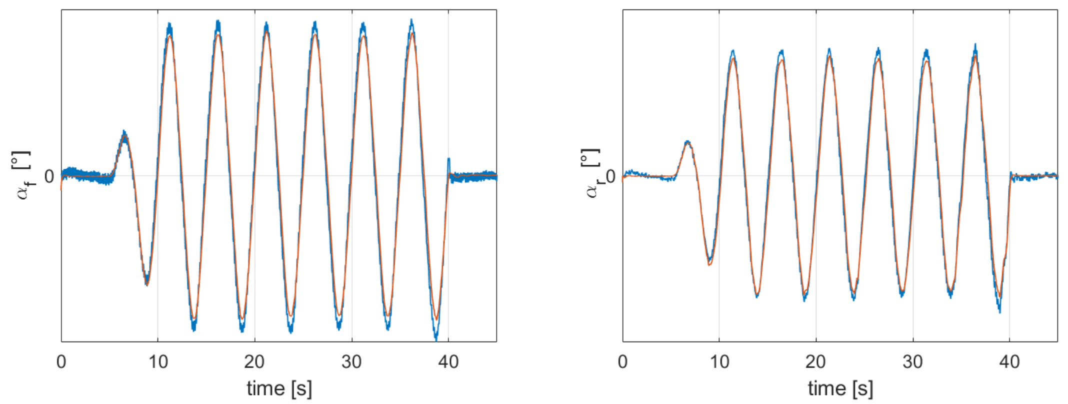

(a) Front axle slip angle (b) Rear axle slip angle

Figure 6.5: Front and rear axle slip angles on a commercial vehicle

are the estimated angles. The only vehicle equipped with the WheelWatch sensors was one of the two commercial vehicles, so only the data relative to it is shown. The estimated angles are almost entirely overlapped with the measured ones, demonstrating the estimator capability. It has to be stressed that the estimator is able to reproduce with a good degree of precision data obtained with expensive dedicated sensor equipment, using as input only data coming from an inertial measurement unit.

Axle lateral forces

The lateral forces for the front and rear axle F_{yf} and F_{yr} for the SimRod vehicle are shown in figure 6.6, together with their respective relative errors. The blue lines in

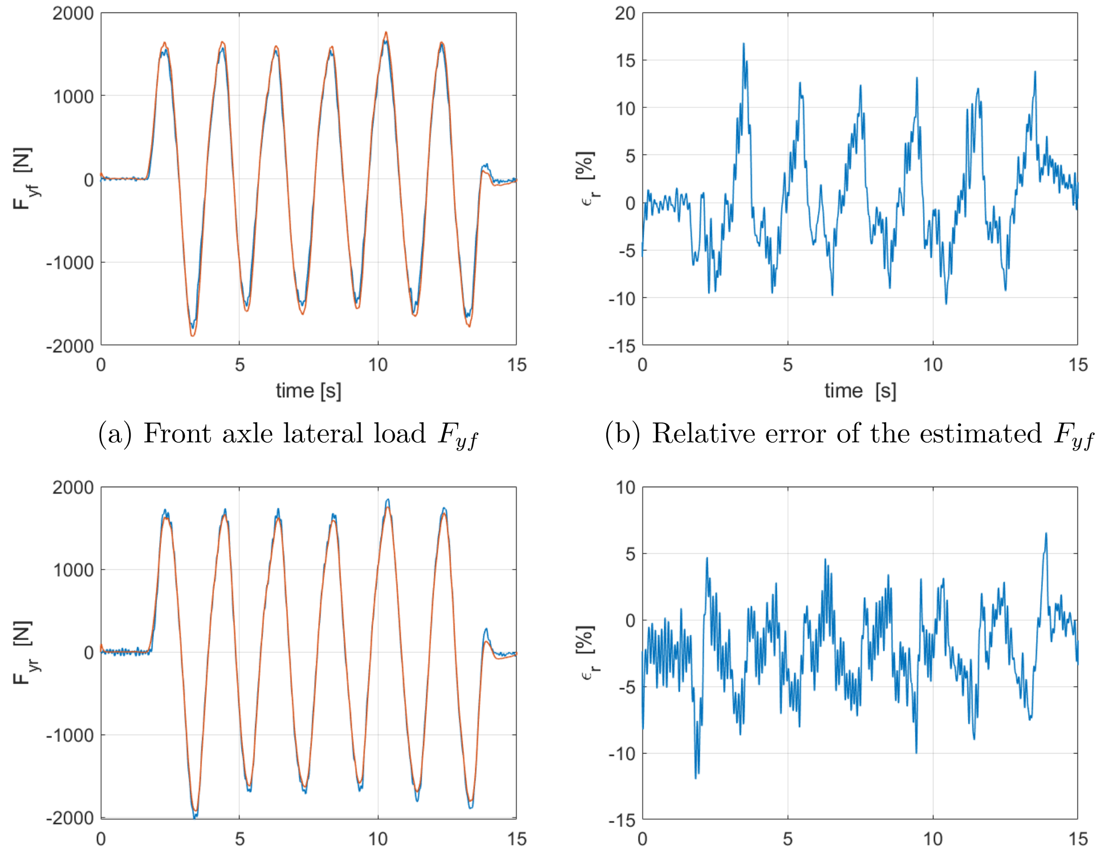

(a) Front axle lateral load F_{yf}

(b) Relative error of the estimated F_{yf}

(c) Rear axle lateral load F_{yr}

(d) Relative error of the estimated F_{yr}

Figure 6.6: Front and rear lateral loads and their respective relative errors

figures 6.6a and 6.6c are the data measured with the sensors and the orange lines are the estimated forces. The estimated and measured data are almost overlapped, meaning that the estimator is able to reproduce both the amplitude and the phase of the real quantity. Once again, results obtained with dedicated and expensive equipment are reproduced by the estimator.

Wheel vertical loads

The vertical loads for each wheel F_{zfl}, F_{zfr}, F_{zrl} and F_{zrr} are shown in figure 6.7, where the blue lines represent the data measured with the strain gauges and the

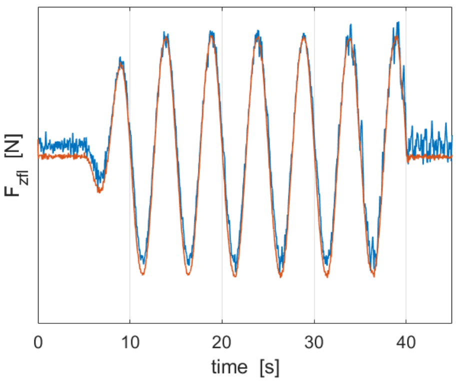

(a) Front left wheel vertical load

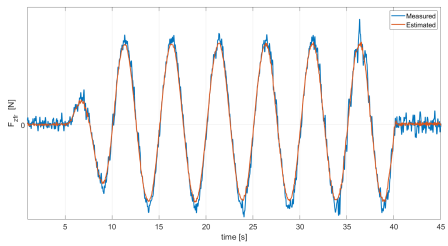

(b) Front right wheel vertical load

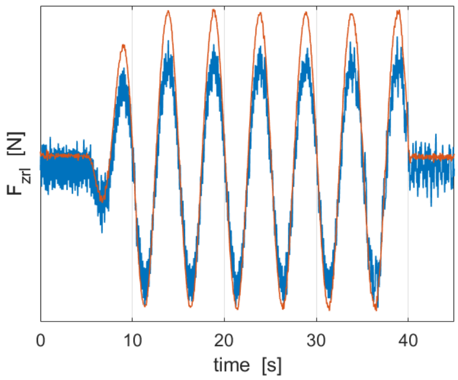

(c) Rear left wheel vertical load

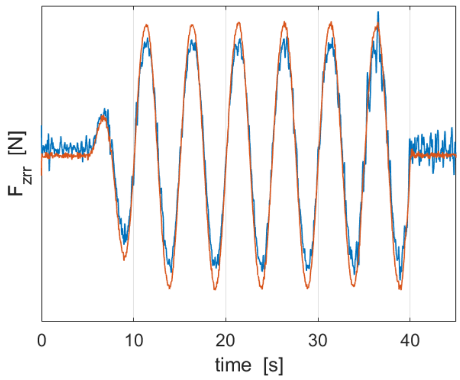

(d) Rear right wheel vertical load

Figure 6.7: Vertical loads on each wheel measured and estimated on a commercial vehicle

orange ones are the estimated loads. The results show a very good fit between the two curves for the wheels at the front axle, while the amplitudes of the estimated forces on the rear wheels have some differences with respect to the measured ones. This is thought to be due to the fact that the two-track model used for the wheel load estimation is not complex enough to capture the actual behavior of the suspensions. It is, however, a promising result since it shows that the wheel loads can be obtained with a good degree of precision using only data relative to the vehicle center of gravity.

Wheel lateral loads

After the wheel vertical loads are computed, they are used to split the front and rear axle lateral forces F_{yf} and F_{yr} in the left and right wheel forces, obtaining F_{yfl}, F_{yfr}, F_{yrl} and F_{yrr}. The results are shown in figure 6.8 (orange lines), compared with the measured data (blue lines).

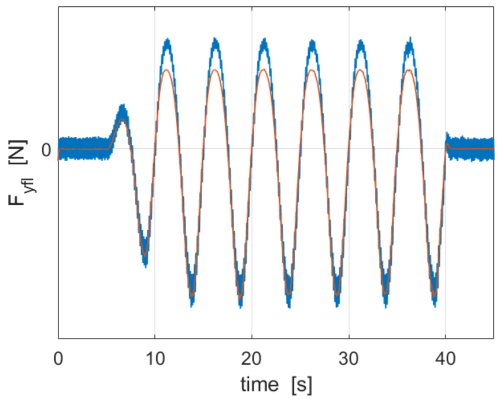

(a) Front left wheel lateral load

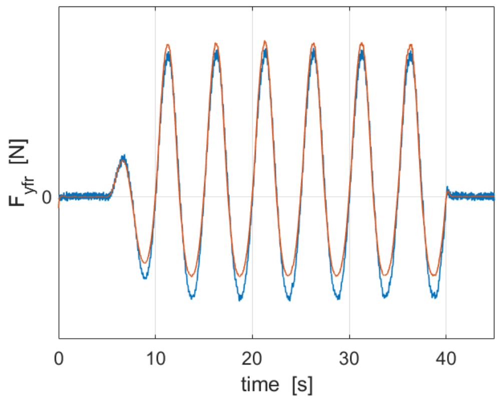

(b) Front right wheel lateral load

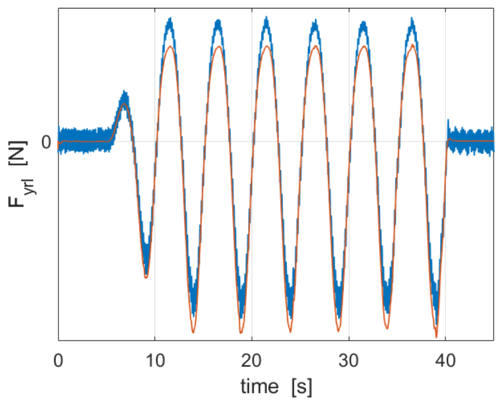

(c) Rear left wheel lateral load

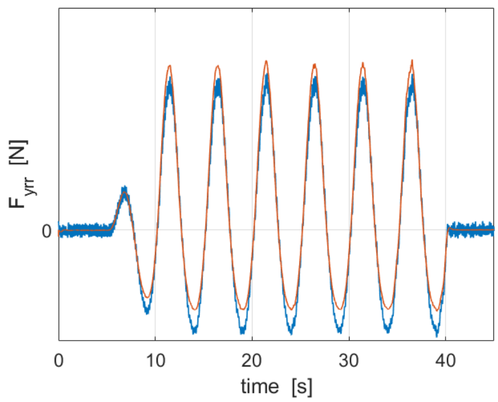

(d) Rear right wheel lateral load

Figure 6.8: Measured and estimated wheel lateral loads for a commercial vehicle

All the estimated curves show a mismatch in amplitude, which is thought to be caused by the ply-steer and tire conicity effects which are neglected here, as well as by the non-perfect estimation of the wheels vertical loads. The results, however, are promising and further work in this direction should help decrease the amplitude error.

6.3 Enhancements of signals at boundary conditions

In this section it is demonstrated that the modular estimator presented in this thesis, aside from expanding the available set of measurements as shown in section 6.2, is used to enhance the quality of signals measured in boundary conditions such as the challenging on-center scenario. In maneuvers with low levels of lateral acceleration, the sensors performance degrades especially regarding the lateral velocity. This is to be expected since in the IMU v_y is obtained by integration of the measured lateral acceleration, making it prone to errors.

The data shown in this section is obtained with sinusoidal maneuvers at constant velocity on a commercial vehicle, since on-center handling maneuvers have not been performed on the SimRod vehicle.

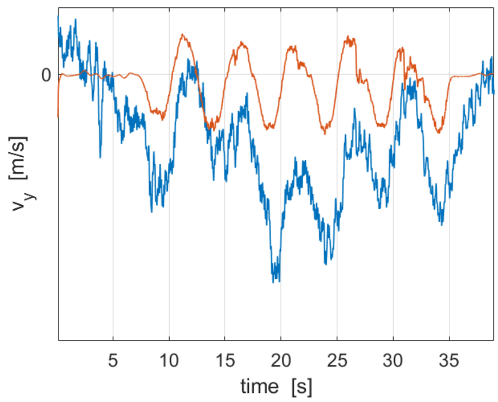

(a) v_y without roll correction

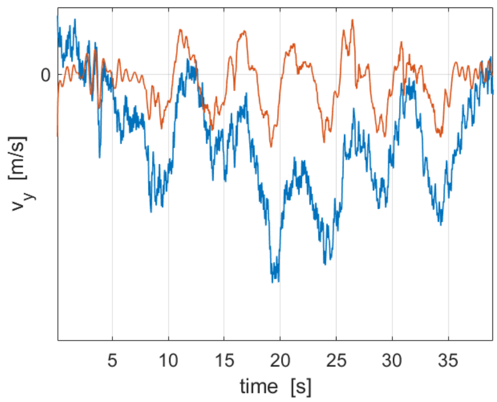

(b) v_y with roll correction

Figure 6.9: Lateral velocity at low levels of lateral acceleration

The blue lines represent the lateral velocity measured with the OxTS IMU, while the orange ones represent the estimated lateral velocity without the roll correction (figure 6.9a) and with the roll correction applied (6.9b). It is clear that the measured v_y is subject to drifting and is not stable. The lateral velocity estimated by the EKF (figure 6.9a) already stabilizes and enhances the quality of the signal to the point where the sinusoidal shape is clearly recognizable. Moreover, by adding the roll correction (figure 6.9b), it is assured that the phase of the estimated signal is correct and that the dynamics content is preserved. In fact, the orange curve in figure 6.9b contains several spikes and what may seem noise, but those are actually small variations of the lateral velocity due to road irregularities or suspension phenomena that are too small to be observed in maneuvers performed at higher levels of lateral acceleration.

The estimator performance does not degrade even for other signals such as the axle lateral forces, which are more complex to measure (the wheel lateral and vertical forces are available only on the other commercial vehicle, which had the K&C testing performed). The axle lateral forces F_{yf} and f_{yr} are shown in figure 6.10,

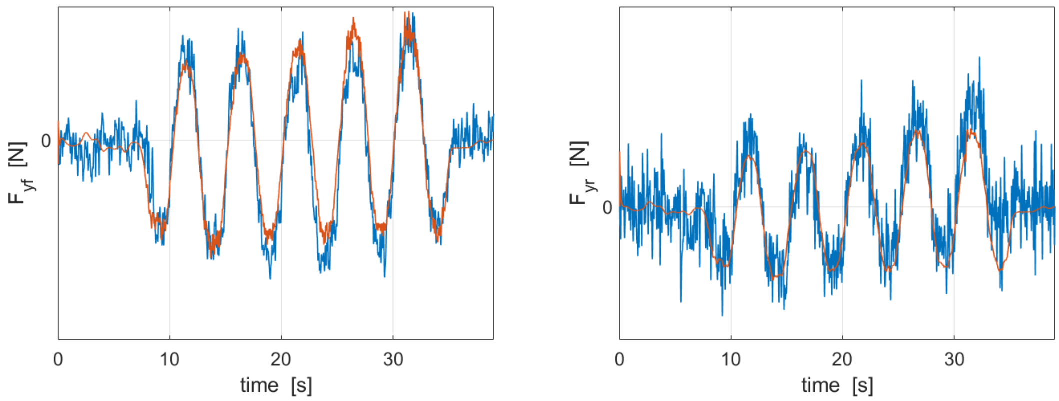

(a) Front axle lateral force

(b) Rear axle lateral force

Figure 6.10: Axle lateral forces at low a_y

where the blue lines are the loads obtained with the strain gauges and load identification method and the orange ones are the results of the estimator. It is remarkable that the estimator reproduces both in amplitude and phase the loads even in a challenging condition such as the on-center one. The dynamics content of the estimated curves is yet to be validated, nevertheless this is a very promising result.

6.4 Practical application

After demonstrating that the estimator can reproduce the results obtained with expensive and dedicated sensor equipment, even in challenging conditions, it has been used in a real application case. The maneuver used in this case is a step steer to the left at constant velocity, performed on a commercial vehicle at medium levels of lateral acceleration using a steering robot and an accelerating and braking robot, to achieve maximum repeatability of the measures. The data shown in this section is the average of seven runs of the same maneuver. The part of the maneuver which has been analyzed is the first transient, highlighted with a black box in figure 6.11.

Measurements were performed on the base version of the vehicle, then a small structural modification was applied and the same measurements were taken again. The difference between the base and modified versions could reportedly be felt

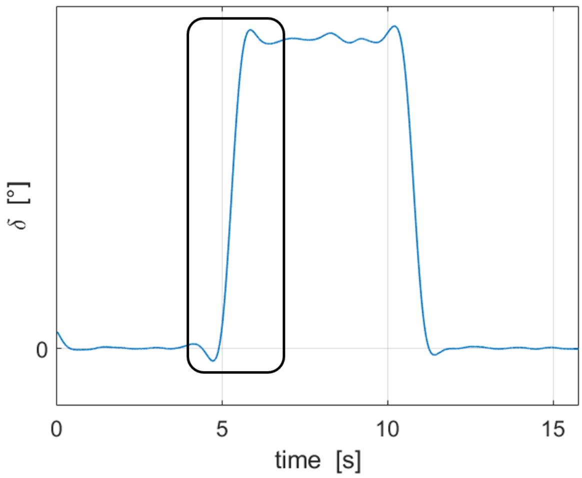

Figure 6.11: Step steer maneuver

even by non-professional drivers when driving the car. When the data was analyzed, small differences were found in the lateral loads build-up and steady state, as highlighted in figure 6.12a. Then, the IMU data of those test drives was run through the estimator, to see whether it could detect the same differences. Figure

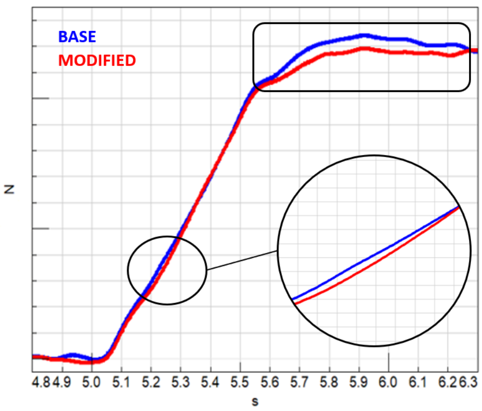

(a) Measured front axle lateral load

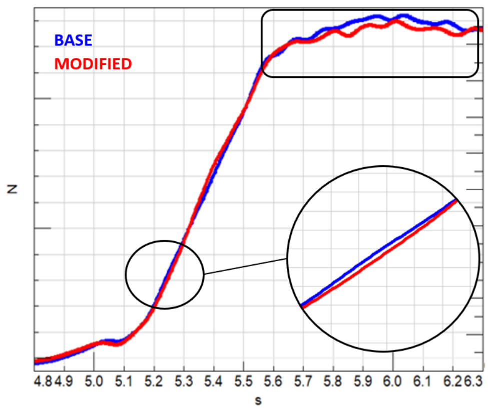

(b) Estimated front axle lateral load

Figure 6.12: Measured and estimated base-modified comparison

6.12b shows the estimated lateral forces for the base and modified vehicle. It is clearly seen that the estimator can capture the steady state difference between the two version, and by taking a closer look at the transient, also the slight difference in time in the loads build-up was captured, although not as well as the physical sensors did. The measured time difference in the loads transient was about 20 ms, while the estimated one only 5 ms. Although it is not captured correctly, this result is still remarkable since it was not expected to be able to see a difference at all using an estimator with input data relative solely to the center of gravity. In future works it is expected to add localized suspension data to improve the precision of the results, with the aim of getting as close as possible to the measurements.

Chapter 7

Conclusions and future work

7.1 Conclusions

The objective of this thesis work was to expand the model-supported response estimation approach, whose project was started in 2017 with the theses of Ricci [8] and Streppa [11], to enable the estimation of additional vehicle dynamics response quantities at low response conditions. This through the use of high precision inertial sensors in combination with vehicle models.

The proposed approach presents a modular estimator based on an extended Kalman filter, where the adopted model is a single-track model coupled with an adaptive linear tire model in which the cornering stiffnesses evolution is modeled with a random walk model.

The most challenging issue has been the estimation of the lateral velocity, since no direct reference was available for it and and also because in maneuvers performed at low levels of lateral acceleration the signal to noise ratio values decrease so that inertial sensors are no longer able to provide reliable measurements. For this reason, an additional model in which the cornering stiffness values are assumed to be constant is introduced, in order to obtain a virtual measurement of the sideslip angle β_{lin} that is used as an additional input, in order to avoid drifting and inaccuracies in the estimates. Then, in order to account for those situations in which the linear model would not produce a reliable value of the sideslip angle, the covariances relative to the cornering stiffnesses and to the virtual sideslip angle are adapted to modify the uncertainty attributed to them.

An estimator based on a Linear Matrix Inequalities problem was used to estimate the wheel steering angle since it was one of the inputs of the EKF and no measurement for it was available.

Then, it was observed that the lateral velocity estimated by the extended Kalman filter showed a time delay with respect to the measured one, so the roll rate measurement was used to correct this. The updated lateral velocity was then used to compute the vehicle sideslip angle.

By combining some of the inputs and outputs of the EKF (equations (2.11) and (2.12)), the front and rear tire slip angles are obtained. They are then multiplied by the estimated cornering stiffnesses to obtain the front and rear axle lateral loads.

Moreover, if the front and rear roll stiffness parameters are known, the vertical loads for each wheel are obtained, which, according to the load proportionality principle, are then used to split the lateral loads on each axle into the left and right wheels.

Going back to what has been said in the problem statement, the reasons behind the interest in virtual sensing are mainly two. The first one is that current detailed testing approaches using physical sensors are elaborate and expensive. To overcome this, a modular vehicle dynamics estimator has been developed, setting the framework for future advancements in this field. The developed estimator has been proven to be able to reproduce with good levels of approximation results obtained with advanced testing. It has been validated on a global level, and in future works will be enhanced to better capture detailed dynamics.

The second reason behind Siemens taking interest in virtual sensing is that reliable testing at on-center condition is a key challenge. It has been demonstrated that the developed estimator increases the stability of data measured at on-center condition, while in future work it will be ensured that the relevant dynamics content is captured.

Finally, the estimator has been applied to a base-modified condition, to see if it could detect the observed differences on a commercial vehicle before and after some modifications have been applied to it. The results show that the estimator captured the significant performance changes, while it did not correctly capture the observed transient changes. This is, however, to be expected since the input data of the estimator is relative solely to the center of gravity.

7.2 Future work

The estimator developed in this thesis work serves as a framework to be expanded in future collaborations. Further work to enhance the estimator capabilities could be done in the following areas:

- **Insertion of specialized or localized test data**
  The insertion of data measured in different locations of the vehicle, such as the suspension struts, is expected to enhance the precision of the measurements as well as their dynamics content. This is expected to improve the wheel loads estimation in particular.

- **Parameters identification**
  By introducing a standardized approach for the identification of certain vehicle

parameters such as the cornering stiffness, the roll center height, the yaw inertia or the roll stiffness, it is expected to obtain more precise and reliable results. This would also reduce the amount of time spent in manually tuning the parameters.

- **Exploration of the estimator capabilities**
  It is yet to be determined whether the estimator can correctly identify and analyze the non-linear behavior of the vehicle in on-center condition. Frequency domain analysis of the estimated data at different levels of lateral acceleration, from medium to very low, will reveal if the non-linear phenomena observed in measured data is correctly captured by the estimator.

Bibliography

[1] L. Liu, S. M. Kuo, and M. C. Zhou, "Virtual sensing techniques and their applications," *Proceedings of the 2009 IEEE International Conference on Networking, Sensing and Control, ICNSC 2009*, pp. 31–36, 2009.

[2] D. Dailey, F. Cathey, and T. Trepanier, "Deployment of a Virtual Sensor System, based on Transit Probes, in an Operational Traffic Management System," no. November, 2006.

[3] Z. Ankara, T. Kammerer, A. Gramm, and A. Schütze, "Low power virtual sensor array based on a micromachined gas sensor for fast discrimination between H2, CO and relative humidity," *Sensors and Actuators, B: Chemical*, vol. 100, no. 1-2, pp. 240–245, 2004.

[4] A. Schütze, A. Gramm, and T. Rühl, "Identification of Organic Solvents by a Virtual Multisensor System with Hierarchical Classification," *Proceedings of IEEE Sensors*, vol. 1, no. 1, pp. 382–387, 2002.

[5] F. Bellas, J. A. Becerra, J. Santos, and R. J. Duro, "Applying synaptic delays for virtual sensing and actuation in mobile robots," *Proceedings of the International Joint Conference on Neural Networks*, vol. 6, pp. 144–149, 2000.

[6] U. Kiencke and L. Nielsen, *Automotive Control Systems*, vol. 59. Springer, 2006.

[7] G. Avino, P. Bande, P. A. Frangoudis, C. Vitale, C. Casetti, C. F. Chiasserini, K. Gebru, A. Ksentini, and G. Zennaro, "A MEC-based Extended Virtual Sensing for Automotive Services," *IEEE Transactions on Network and Service Management*, pp. 1–1, 2019.

[8] M. Ricci, "Vehicle parameters estimation techniques in low response maneuvers." 2018.

[9] K. D. Norman, "Objective evaluation of on-center handling performance," *SAE Technical Papers*, 1984.

[10] F. Naets, S. Van Aalst, B. Boulkroune, N. E. Ghouti, and W. Desmet, "Design and experimental validation of a stable two-stage estimator for automotive sideslip angle and tire parameters," *IEEE Transactions on Vehicular Technology*, vol. 66, no. 11, pp. 9727–9742, 2017.

[11] G. Streppa, "Rotational motion identification from MEMS inertial sensors." 2018.

[12] H. B. Pacejka, “Vehicle System Dynamics : International Journal of Vehicle Mechanics and Mobility,” *International Journal of Vehicle Mechanics and Mobility*, no. August 2012, pp. 37–41, 2008.

[13] M. Abe, *Tire Mechanics*. 2015.

[14] M. C. Best, T. J. Gordon, and P. J. Dixon, “Extended adaptive Kalman filter for real-time state estimation of vehicle handling dynamics,” *Vehicle System Dynamics*, vol. 34, no. 1, pp. 57–75, 2000.

[15] A. Albinsson, F. Bruzelius, and M. Jonasson, “Tire Force Estimation Utilizing Wheel Torque Measurements and Validation in Simulations and Experiments,” *International Symposium on Advanced Vehicle Control*, pp. 294–299, 2014.

[16] R. E. Kalman, “A new approach to linear filtering and prediction problems,” *Journal of Fluids Engineering, Transactions of the ASME*, vol. 82, no. 1, pp. 35–45, 1960.

[17] M. I. Ribeiro, “Kalman and Extended Kalman Filters : Concept , Derivation and Properties,” *Institute for Systems and Robotics Lisboa Portugal*, no. February, p. 42, 2004.

[18] S. Boyd, L. El Ghaoui, E. Feron, and V. Balakrishnan, *Linear Matrix Inequalities in System and Control Theory*.

[19] S. V. Aalst, “Vehicle Dynamics Estimation,” 2018.

[20] M. Acosta, S. Kanarachos, and M. E. Fitzpatrick, “A virtual sensor for integral tire force estimation using tire model-less approaches and adaptive unscented Kalman filter,” *ICINCO 2017 - Proceedings of the 14th International Conference on Informatics in Control, Automation and Robotics*, vol. 1, no. August, pp. 386–397, 2017.

[21] OxTS, “RT GNSS-aided inertial measurement systems,” no. June, p. 143, 2018.

[22] Kistler, “Correvit S-Motion,” pp. 2–4, 2018.

[23] “AICON Wheel Watch.”

[24] Kistler, “RoaDyn ® S660,” 2016.

[25] N. Mango, “Measurement & calculation of vehicle center of gravity using portable wheel scales,” *SAE Technical Papers*, 2004.

[26] D. M. Bevly, J. Ryu, and J. C. Gerdes, “Integrating INS sensors with GPS measurements for continuous estimation of vehicle sideslip, roll, and tire cornering stiffness,” *IEEE Transactions on Intelligent Transportation Systems*, vol. 7, no. 4, pp. 483–493, 2006.

[27] R. A. Bixel, G. J. Heydinger, N. J. Durisek, D. A. Guenther, and S. J. Novak, “Developments in vehicle center of gravity and inertial parameter estimation and measurement,” *SAE Technical Papers*, no. 41 2, 1995.